Mémoire

Auteur : Gérard, Adrien
Promoteur(s) : 24616; Alvera Azcarate, Aida
Faculté : Faculté des Sciences
Diplôme : Master en océanographie, à finalité approfondie
Année académique : 2023-2024
URI/URL : http://hdl.handle.net/2268.2/20883

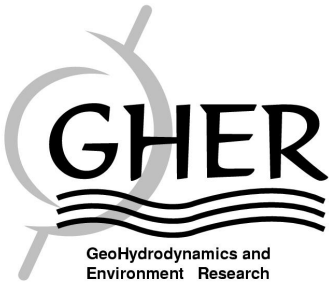

University of Liège

Master's Degree Thesis

Variability of deep currents above the Mid-Atlantic Ridge in the South Atlantic

Author:
Adrien Gérard

Supervisor:
María Dolores Pérez Hernández

Co-Supervisor:
Aida Alvera Azcarate

Review panel:
Alexander Barth
Aurélia Hubert
Charles Troupin

A thesis submitted in fullfillment of the requirements for the

Master's Degree in Oceanography

in the

Faculty of Sciences

June, 2024

According to the rules imposed by the jury of the Master in Oceanography, this document must not exceed 50 pages in Times 12 or an equivalent font.

Acknowledgements

I would first like to thank María Dolores Pérez Hernández, my supervisor, for welcoming me into the IOCAG research group and supporting me in this work. I would also like to thank Aida Alvera Azcarate, who made this collaboration with the University of Las Palmas de Gran Canaria possible and who has also followed this work from start to finish. Next, I extend my thanks to all the members of IOCAG for their warm welcome, their patience with me as I practiced Spanish, and for their answers to my questions. Finally, I would like to thank Alberto Alcalá Verdugo, who integrated me into the university and with whom I spent a lot of time discussing the SAGA project results and about our cultures.

Contents

Abstract

Due to its geographical location, the South Atlantic subtropical gyre plays an important role in the Atlantic Meridional Overturning Circulation (AMOC), which controls the Earth's climate by redistributing water masses, heat, and freshwater in the Atlantic. This thesis therefore studies the data collected by a mooring between April 2021 and April 2023, located on the eastern flank of the Mid-Atlantic Ridge (-21.631°N, -9.967°E), as part of the larger South Atlantic GAteway project. The water mass in which the mooring was placed (from 2351 m to the seafloor at 4407 m) was identified as the North Atlantic Deep Water (NADW). The currents measured in the upper part of the mooring, with a mean current weakly directed westward, were attributed to the influence of the South Equatorial Current, while the deeper currents, with a mean current directed eastward, were attributed to the transport of NADW over the Mid-Atlantic Ridge at these latitudes. Finally, sea level anomalies were compared with the variability in currents and temperature, and their synchronous variation along the depth was identified as disturbances from the westward propagation of long baroclinic Rossby waves.

1 Introduction

Chapter Contents

The Atlantic Meridional Overturning Circulation (AMOC) is the Atlantic branch of the planetary Meridional Overturning Circulation (MOC), formerly known as the thermohaline circulation. Its origins lie in differences in density resulting from differences in temperature and salinity, although we now know that wind field and tidal stirring also play a vital role (Wunsch, 2002). The AMOC plays a key role in climate by redistributing the mass, heat and fresh water of the Atlantic. Given the challenges posed by Climate Change, understanding the mechanisms of the AMOC and its evolution will be essential in the years to come.

By its position, the South Atlantic Ocean is important for the AMOC because it connects the Atlantic Ocean to other ocean basins. However, as mentioned in Garzoli and Matano, 2011, our difficulties in estimating the mass balance of the South Atlantic stem directly from our lack of knowledge and observations of its circulation and in particular its subsurface circulation. It is therefore necessary to extend our observation systems in order to increase our knowledge of the AMOC and its impact in climate. The fractures in the topography that concentrate the deep circulation should be given priority for observation because they influence the links between the different ocean basins, such as the Drake Passage and the mid-Atlantic Ridge.

This thesis has been developed within the framework of the South Atlantic Gateways project (SAGA; https://uoc-csic.ulpgc.es/project/saga-south-atlantic-gateway-global-conveyor-belt) funded by the Spanish Ministry of Science. The aim of this project is to quantify and monitor the AMOC in the South Atlantic, and more specifically the interior zonal flow between the eastern and western basins of the Mid-Atlantic Ridge (MAR). To do this, they deployed moorings equipped with instruments to measure the current and compare these results with those obtained by Pressure Inverted Echo Sounder (PIES).

1.1 The Atlantic Meridional Ocean Circulation (AMOC)

The ocean, with its great thermal inertia, is a major contributor to global heat transport. In fact, the heat capacity of the first two metres of the oceans is equivalent to that of the entire atmosphere, showing the extent to which the quantity of heat in the ocean dominates our planet's energy reservoir (Sévellec and Sinha, 2018). As a result, the ocean is an essential component of the climate system, exchanging heat and gases with the atmosphere (Houghton, 1996, Macdonald and Wunsch, 1996).

The AMOC is the Atlantic branch of the global overturning circulation (Figure 1.1). It consists of a warm current of near-surface water which moves northwards and releases its heat to the atmosphere. This loss of buoyancy in the high latitudes of the North Atlantic carries this surface water downwards to form the North Atlantic Deep Water (NADW), the deep southward branch of the AMOC (Srokosz et al., 2012). However, the AMOC is also dynamic over time, varying over periods ranging from seasons to decades (Desbruyères et al., 2019, Moat et al., 2020, Sévellec and Sinha, 2018).

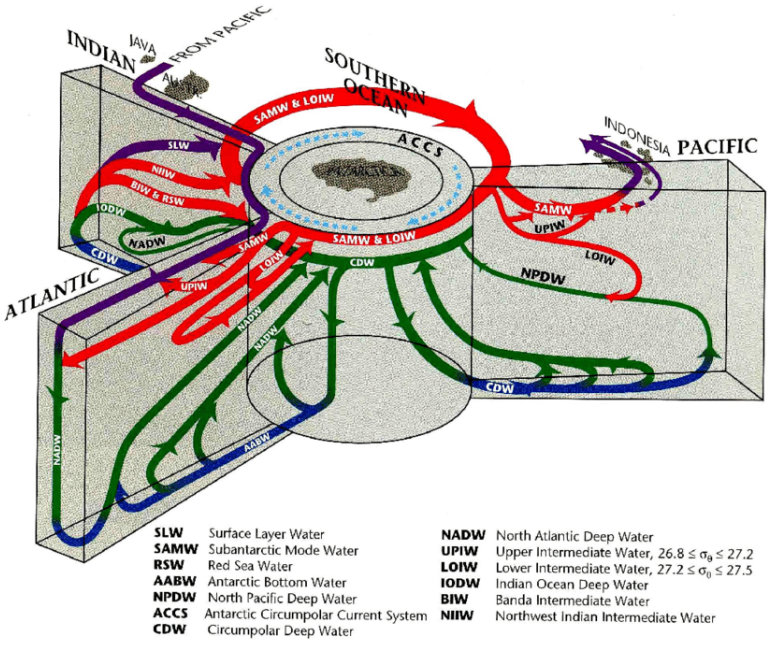

Figure 1.1: Three-dimensional meridional global ocean slices that depict NADW formation and interbasin flow (image from Schmitz, 1996).

In order to continuously collect additional data on the evolution of the AMOC, moorings have been deployed at strategic latitudes in the Atlantic for measurements lasting

from a few days to a few months. We can cite OSNAP (https://www.o-snap.org/about-us/related-programs/) (Lozier et al., 2017), RAPID/MOCHA/WTBS array (Cunningham et al., 2007, Johns et al., 2011), MOVE (Kanzow et al., 2006), TSAA (Hummels et al., 2015) and SAMBA (Meinen et al., 2013) as projects conducted in the Atlantic Ocean that have studied AMOC variations on daily, monthly or seasonal time scales (Frajka-Williams et al., 2019, McCarthy et al., 2020). However, the first projects date from the 2000s, making it impossible to study the AMOC before this decade and then the low-frequency variability. Thus, comparison of hydrographic data remains the only means of analysing differences in transport over longer periods.

In 2000, Ganachaud and Wunsch, 2000 combined all the available hydrographic observations of transoceanic sections from the World Ocean Circulation Experiment (WOCE) project of transoceanic sections with data from climatological winds and biogeochemical budgets to carry out a global inverse box model. They found no decrease in the production rate of AABW, contrary to what is stated in Broecker et al., 1999. Ganachaud and Wunsch, 2000 also mention that to improve the model for a climate-averaged view, the inclusion of meridional sections could improve spatial resolution as well as the addition of time-averaged data to reduce errors introduced by ocean variability from daily to interannual scales.

Recent publications have stated a potential weakening of the AMOC due to anthropogenic global warming (Caesar et al., 2018, Rahmstorf et al., 2015), but no measurements have yet confirmed this prediction. The subject of a potential weakening of the AMOC is very important and the comparison of models with measurements is crucial to the debate. This is why Caínzos et al., 2022 used southern and zonal transect data from the international WOCE and GO-SHIP projects over the last 30 years to produce 3 inverse box models, one for each of the last 3 decades. The result of the inverse box model can be seen in Figure 1.2 that shows two counter-rotating overturning cells (arrows at bottom). The upper loop is closed by vertical transport, which consists of the densification of the surface waters of Surface North Atlantic Central Water (NACW) in the subpolar North Atlantic (McCartney and Talley, 1984) and the upwelling of NADW in the subtropical gyre of the South Atlantic Ocean. In the abyssal loop, part of the NADW sinks in the Southern Ocean (Wefer et al., 2012), then flows northwards again as Antarctic Bottom Water (AABW) and finally upwells in the subtropical North Atlantic. Overall, the northward transport of the surface and bottom layers of the ocean is offset by the southward transport of the deep layer (Kersalé et al., 2020).

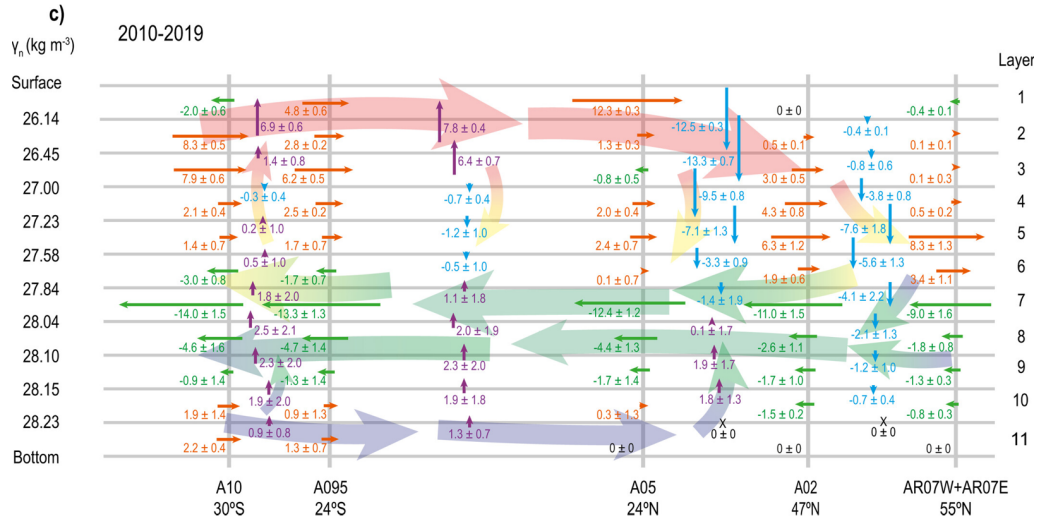

Figure 1.2: Vertical and meridional schematic of the circulation in the Atlantic Ocean for the 2010-2019 decade (only one has been chosen for more clarity). The gray horizontal lines mark the neutral density interphases, and the gray vertical lines are the position of each zonal section at their nominal latitude. The horizontal mass transport (1 Sverdrup (Sv) = 106 $m^3\ s^{-1} \approx 109\ kg\ s^{-1}$) is represented with horizontal arrows, in orange for northward (positive) transport and green for southward (negative) transport. Black dots in the North Atlantic appear in layers with null transport. The vertical transport between two sections in the interphase between two layers is represented with vertical arrows, in violet for upward (positive) transport and blue for downward (negative) transport. Black crosses represent layers with no vertical transport (image from Caínzos et al., 2022).

Regarding a potential weakening of the AMOC, the three inverse solutions show no difference in transport for any layer between the three decades. However, it should be borne in mind that the inverse solutions evaluated by measurements are limited to short time intervals. As with other global climate inverse models over the first decade of this paper, no AMOC decay has been calculated (Ganachaud, 2003, Lumpkin and Speer, 2007, Macdonald, 1995, Sloyan and Rintoul, 2001). In addition, Fu et al., 2020 also did not observe any weakening of the AMOC in the subpolar North Atlantic in his reconstruction of the last three decades.

1.2 South Atlantic Currents

The circulation in the first 1000-1500 metres in the South Atlantic Ocean is conditioned by surface wind forcing in the Atlantic, generating Ekman pumping, subduction and obduction (Talley, 2011). The circulation therefore depends on whether the system is tropical, subtropical or subpolar. In the intense subtropical western boundary current, the wind-driven surface currents barely reach the ocean floor. However, outside the

Deep Western Boundary Current (DWBC), the circulation below the pycnocline is dictated by buoyancy forcing and the overturning circulation. These currents are very slow and can easily be masked by turbulence (Talley, 2011). Furthermore, these deep circulations are directly impacted by bathymetry, which makes them more complex (Talley, 2011).

On the scale of the South Atlantic, the upper layer of warm water moves northwards to compensate for the southward transport of cold, deep water formed in the high latitudes of the North Atlantic. The intermediate water is heated and upwelled around the equator and then participates in the convection circulation of the deep waters (Boebel et al., 1999).

1.2.1 Upper and intermediate circulation

The surface circulation (0-100 m) in the South Atlantic Ocean is made up of the eastward-flowing Antarctic Circumpolar Current (ACC), an anticyclonic subtropical gyre and a cyclonic tropical gyre. In the tropics, the surface of the South Atlantic Ocean is covered by the mixed layer known as Tropical Surface Water. This layer is bordered to the south by the seasonal thermocline mixing layer. Below these, three subsurface water masses divide the upper layer of the tropical and subtropical South Atlantic. The most superficial is the South Atlantic Central Water (SACW) from about 100 to 500 m. It is relatively warmer and saltier than the Antarctic Intermadiate Water (AAIW, about 500 to 1200 m) it overlies. The deepest water mass in the upper layer is the Upper Circumpolar Deep Water (UCDW, at about 1000 m above the tropics) (Stramma and England, 1999).

The subtropical gyre, which we'll be looking at more closely as it concerns the geographical region of interest in this study, is bordered to the west by the southward-flowing Brazil Current, to the south by the South Atlantic Current (SAC), to the east by the Benguela Current system (BCS) and to the north by the South Equatorial Current (SEC), which splits in two as it reaches the Brazilian coast between the Brazil Current and the northward-flowing North Brazil Current (NBC). A pattern of the South Atlantic upper layer circulation is displayed in Figure 1.3.

The South Atlantic subtropical gyre is forced by the anticyclonic wind forcing which causes Ekman pumping and Sverdrup transport across the South Atlantic (Talley, 2011). The Brazil Current is a western boundary flowing southwards and has a narrow return

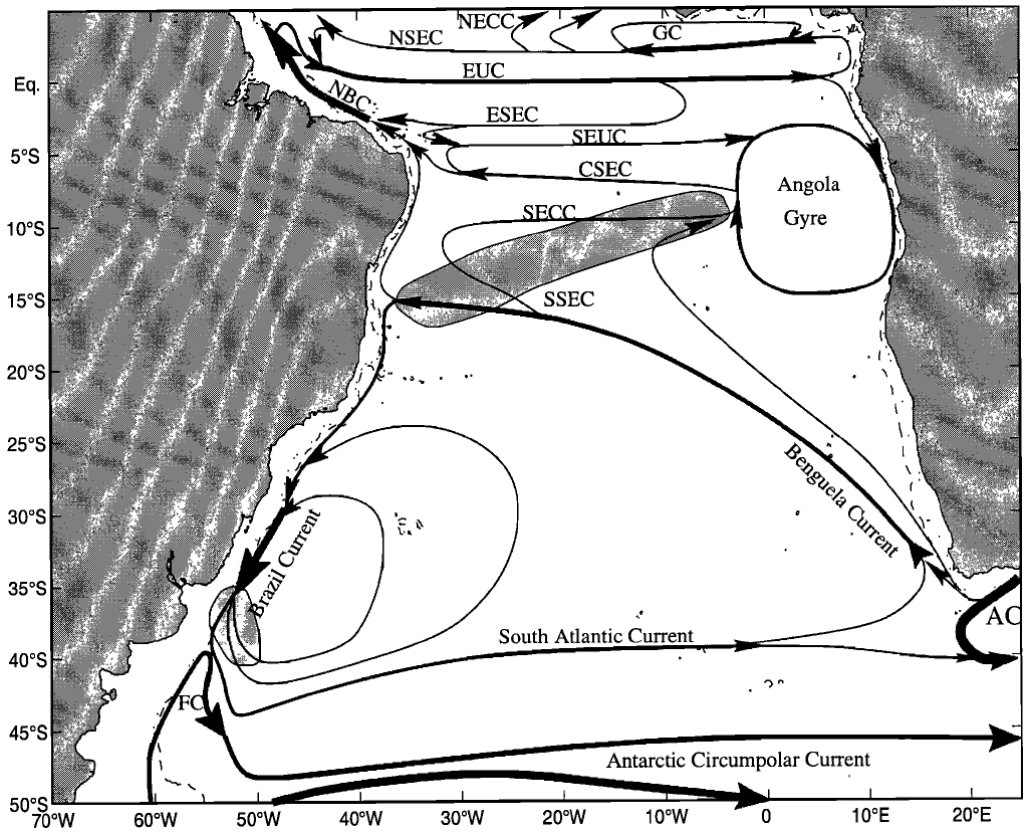

Figure 1.3: Schematic representation of the geostrophic currents of the first 100 meters in the South Atlantic Ocean. The following abbreviations are explained: Falkland Current (FC), Agulhas Current (AC), South Equatorial Current (SEC), with the northern (NSEC), equatorial (ESEC), central (CSEC) and southern (SSEC) branches, North Brazil Current (NBC). The topography for 200-m depth is shown as a dotted line and that for 1000-m depth is shown as a short-dashed line. Image from Stramma and England, 1999.

current east of it. The South Atlantic subtropical gyre stands out from the other southern subtropical gyres because it is important for the global overturning circulation as it transports northwards the surface waters which will form the NADW in the northern seas and the Labrador Sea (Talley, 2011). In addition, the South Atlantic subtropical gyre is linked to the Indian subtropical gyre through the Agulhas leakage whose system is periodically dominated by mesoscale nonlinear dynamics such as Angulhas Rings, eddies and filaments (Beal et al., 2011). Models indicate that variations in the strength of the Agulhas leakage have an impact on the strength of the AMOC (Weijer et al., 2002, Knorr and Lohmann, 2003, Biastoch et al., 2008) and that a permanent change could be responsible for a modification of the stratification of the Atlantic basin and a tilting of the AMOC towards another stable state involving in turn major climatic modifications (Weijer et al., 2002, Weijer et al., 2001).

The largest net source of northward transport of surface water is the Indian Ocean via the BCS and the Agulhas Rings. Another significant part comes from the Pacific through the Drake Passage, bringing slightly denser near-surface waters called Subantarctic Mode Water (SAMW) and AAIW (Talley, 2011). The subantarctic front (SAF) separates the subtropical gyre from the Antarctic circumpolar current (ACC). The SAF enters the Atlantic via the Drake Passage and turns north via the Malvinas Current, where it meets the Brazil Current off the Brazilian coast at around 36-38°S, the Brazil-Malvinas confluence. The two currents turn eastwards to cross the South Atlantic, while retaining their own identities. The SAF thus crosses the Atlantic and then the Indian Ocean at around 50°S (Talley, 2011).

On the east side of the Subtropical Gyre, we find the connection with the Indian Ocean. The Benguela Current extends from the southern tip of Africa, Cape Agulhas at 34°S to 14°S (Strub et al., 1998). It differs from the eastern boundaries of the other subtropical gyres in that it plays a role in the transport of warm water in the Global Overturning Circulation and has a source of warm, highly saline water at its polar extremity. The Benguela Current is fed mainly by the South Atlantic Current, but also by the warm Aghulas Current and, during disturbances in the subtropical front, by water from the Subantarctic Surface Current (Shannon et al., 1989). At its northern end, the Benguela Current meets the warmer Angola Current, forming the Angola-Benguela Front near Cape Frio at around 16°S (Strub et al., 1998).

The Agulhas Rings are solid bodies in rotation up to their extremities where the maximum speed of rotation is located. Agulhas Rings are anticyclonic bodies of water that are warm and salty compared with the surrounding South Atlantic and form when the Agulhas Current retroflects. Around 6 Agulhas Rings are formed each year with a diameter of 100 km to 400 km and drift west-north-west across the South Atlantic (their drift is more zonal than the Benguela Current), around 3 of which reach the Brazilian coast and continue into the NBC (Gordon, 2003). Their maximum rotation speed can reach 100 cm/s at the surface and 10 cm/s at a depth of 4,000 metres.

Intermediate circulation

L. Larqué et al. (Larqué et al., 1997) carried out a multi-parameter analysis (temperature, salinity, dissolved oxygen, nutrients) along conductivity-temperature-depth (CTD) hydrographic transects of the South Atlantic Ventilation Expirement (SAVE). They then used these parameters in an inverse model to quantitatively assess the composition in

the major source water types in the sample and thus evaluate the movement of each water mass.

SACW circulation is very similar to surface circulation. The SACW is transported eastwards by the SAC, where part of it contributes directly to feeding the Benguela Current, while another part passes through the southern Agulhas Current to the Indian Ocean before looping back into the Atlantic (Gordon and Bosley, 1991). The SACW then flows into the Benguela Current and then the SEC until it reaches the Brazilian shelf, where it is carried towards the equator by the North Brazil Undercurrent and the North Brazil Current. A plot of its circulation is shown in Figure 1.4 (Stramma and England, 1999).

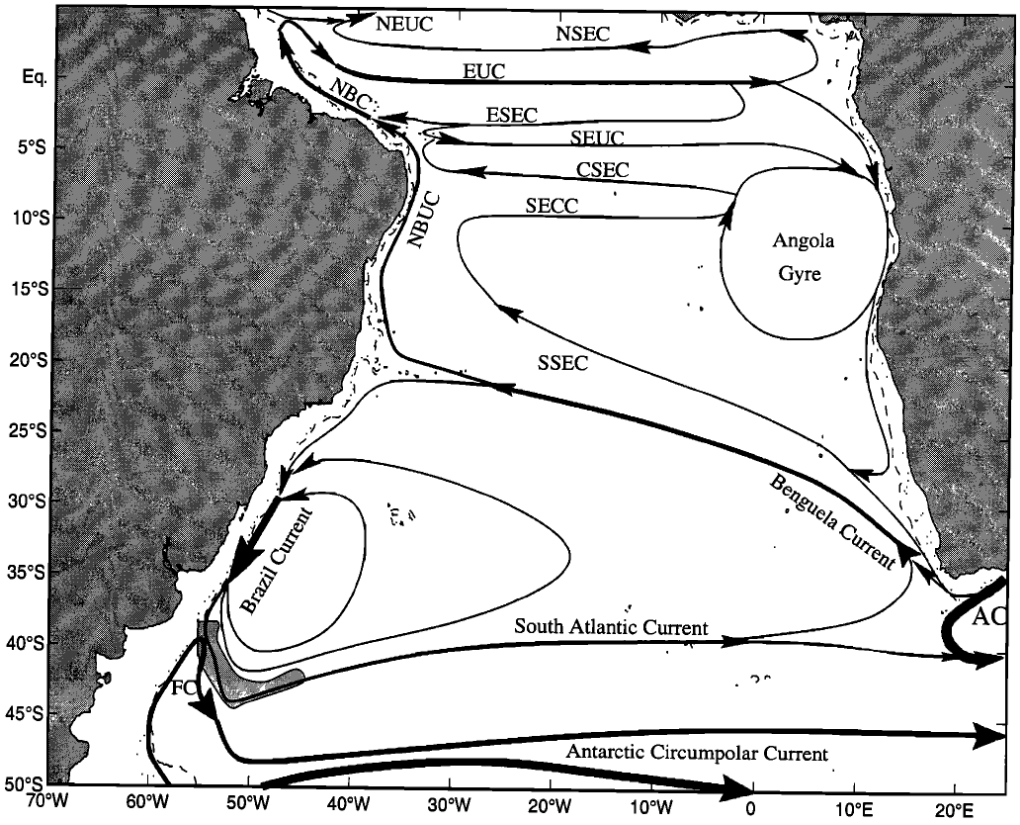

Figure 1.4: Schematic representation of the geostrophic currents at the South Atlantic Central Water (SACW) layer (about 100 to 500 m). Current names and topography are as in Figure 1.3 with in addition the North Brazil Undercurrent (NBUC). Image from Stramma and England, 1999.

In the South Atlantic, the AAIW extends between 300 and 1500 metres, with its thickness varying according to latitude. Its circulation is largely influenced by the sur-

face circulation (Larqué et al., 1997). Initially, Wüst (Wust, 1935) proposed that most of the northward transport of the AAIW took place in the Western Boundary up to the equator, but research has shown that northward transport takes place only in the Western Boundary south of 40°S in the Malvinas Current and north of 25°S (Taft, 1963, Buscaglia, 1971, Reid et al., 1977, Evans and Signorini, 1985, Reid, 1989). South of 40°S, this lightly salted and recently ventilated intermediate water from the ACC enters the South Atlantic and encounters older, saltier recirculated intermediate water in the Brazil-Falkland Confluence Zone as depicted in Figure 1.5. This mixture of intermediate waters is transported eastwards by the SAC of the subtropical gyre (Peterson and Stramma, 1991). Much of this intermediate water is recirculated north-westwards by the SEC of the subtropical gyre. During this process, the intermediate water is joined at the eastern boundary by water from the Indian Ocean. The return current brings the intermediate waters back to the Brazilian coast at around 30°S and divides the intermediate waters into two limbs. One flows northwards to the equator in a narrow western boundary current under the Brazil Current, while the other branch is recirculated southwards (Reid, 1989, Warner and Weiss, 1992).

Less salty, low in oxygen and rich in nutrients than the NADW, the Circumpolar Deep Water (CDW) enters the Argentine Basin via the Drake Passage and its body remains united as it moves northwards to the Subtropical Front at 40-41°S. Beyond this, the CDW splits in two, with the Upper CDW wedged between the AAIW and the NADW and the Lower CDW between the NADW and the oxygen-rich Weddel Sea Deep Water (Antarctic Bottom Water). The CDW then passes into the Brazile Basin via the Vema Channel and Hunter Channel and along the Lower Santos Plateau (Speer and Zenk, 1993). At 4000 dbar in the Cape Basin south of Walvis Ridge, the circulation appears to be cyclonic (Talley, 2011).

1.2.2 Deep and bottom circulation

Slow and deep circulations is still poorly understood due to the lack of direct measurements at such depths. These great depths also mean that currents are mainly impacted by bathymetry, bypassing the topography, which also creates mixing (Talley, 2011). As a result, models have difficulty in representing this circulation because of the lack of observations and the complexity of the topography. Mid-ocean ridges confine the bottom waters to their basin. Nevertheless, fractures in the ridges allow local exchanges from one basin to another, which can be intense and turbulent. The properties in the

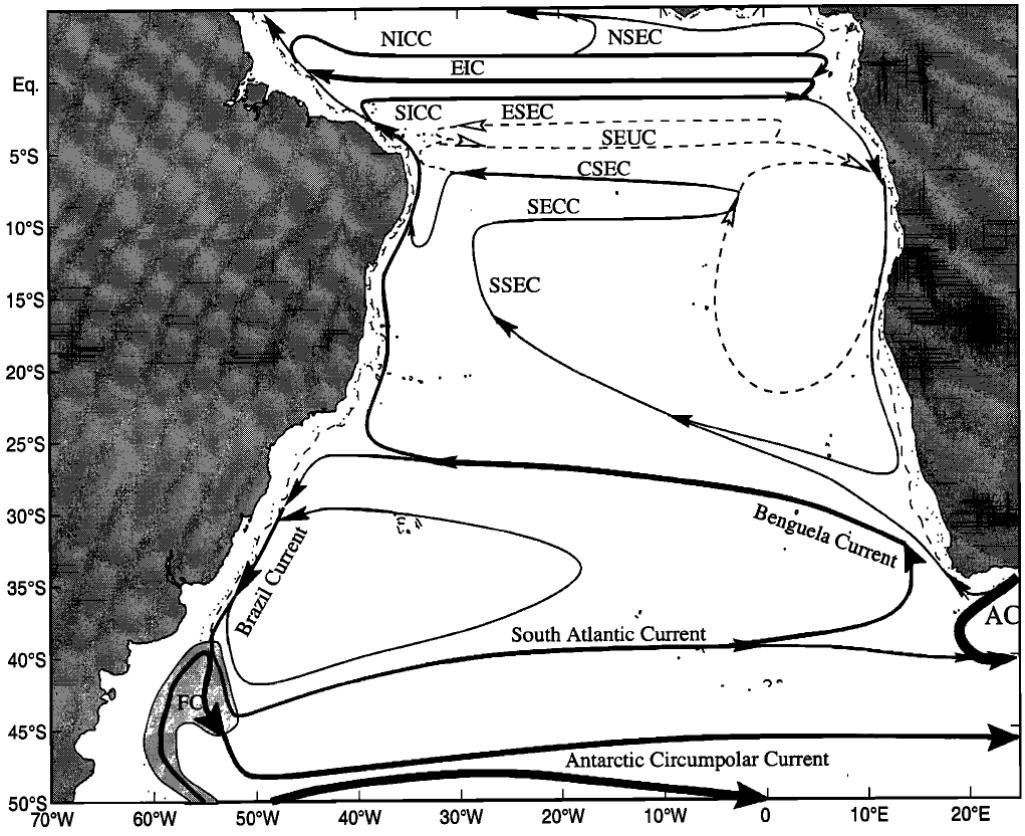

Figure 1.5: Schematic representation of the geostrophic currents at the Antarctic Intermediate Water (AAIW) layer (about 500 to 1200 m). Current names and topography are as in Figure 1.3. Image from Stramma and England, 1999.

basin downstream of the fracture tend to homogenise. The main fractures that allow the passage of Deep and Bottom Water are the Vema and Hunter Channel, which lead the AABW northwards from the Argentine Basin to the Brazile Basin, the Namib Col in the Walvis Ridge, which leads NADW and AABW south-eastwards from Angola Basin into the Cape Basin, and the Romanche fracture zone in the MAR at the equator, which leads NADW and AABW eastwards (Talley, 2011). The Figure 1.6 shows this South Atlantic bathymetry.

The NADW crosses the equator and follows the continent slope until 25°S where it separates and a part of which turns eastward towards South Africa. Below the AAIW, the NADW is limited to the south at around 35°S-40°S where it meets the CDW as depicted in Figure 1.6 (Larqué et al., 1997). In comparison, the NADW signal is weaker on the eastern side of the MAR where it is less salty and less oxygenated, although on this side the NADW reaches the ocean bottom in the Sierra Leone and Angola Basins (Larqué et al., 1997). At 2500 dbar, a residue of the Brazil-Malvinas Confluence is still

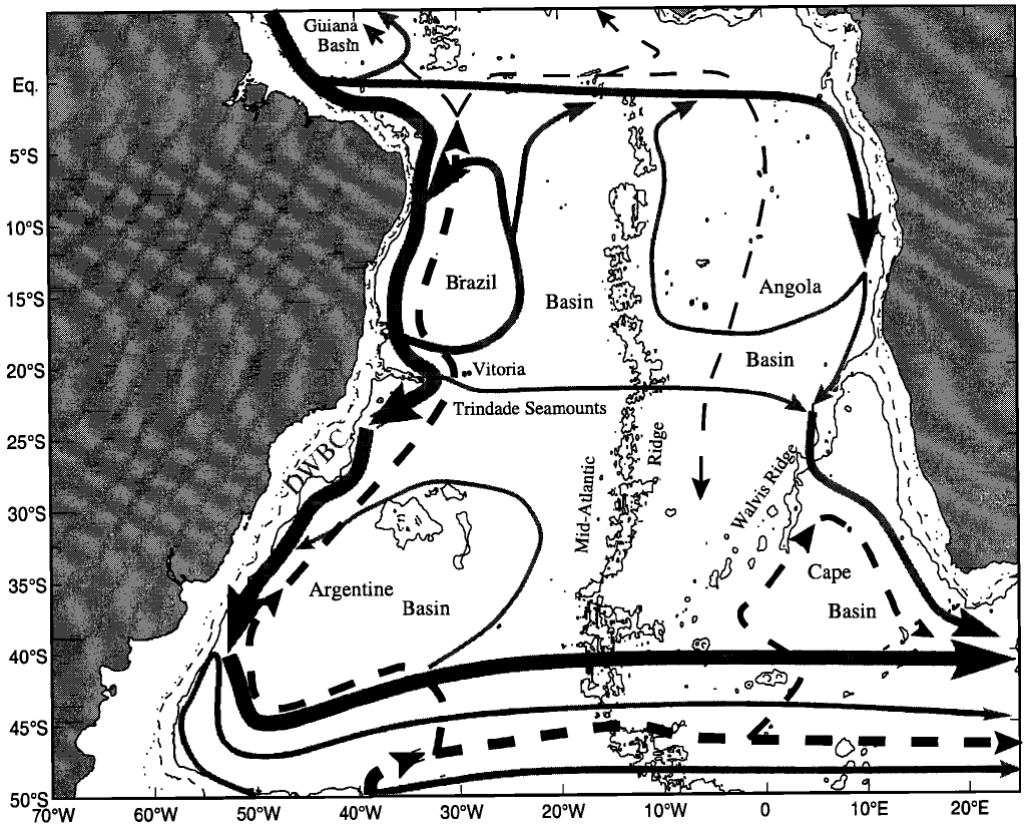

Figure 1.6: Schematic representation of the North Atlantic Deep Water (NADW) water flow near 2000 m depth. Topography is as in Figure 1.3 with in addition the 3000 m depth contour shown as a thin solid line. Image from Stramma and England, 1999.

observable and at the same depth, below the Benguela Current, a current follows the African coast polewards and transfers part of the NADW to the Indian Ocean by flowing northwards along the Indian DWBC while another part is injected into the ACC (Talley, 2011).

The Weddel Sea Deep Water is the densest water in CDW, it is also the coldest and most nutrient-rich in the water column (Reid, 1989). The WSDW is light enough to pass the Drake Passage and then the Vema Channel, but too heavy to cross the MAR and enter the Angola Basin. After the Vema Channel, the Upper WSDW (UWSDW) mixes strongly with the LCDW giving water influenced by both water masses. However, a slight influence from the UWSDW is observed between the equator and 3°S as the WSDW is able to cross the MAR through the Romanche Fracture Zone and the Chain Fracture Zone, with another part of the current continuing northwards across the equator (Larqué et al., 1997). The branch heading east is joined by the NADW to head south again. It is this water that fills the north-east basin of the South Atlantic, as

Walvis Ridge prevents any inflow of abyssal water from the south (Talley, 2011).

Direct measurements have observed large temporal variations in the AABW in the DWBC, which crosses the South Atlantic to the north. The transformations that this current undergoes are in the passage from the Argentine basin to the Brazile basin at 32°S to the Rio Grande Rise, the deepest part of which is confined to the Vema and Hunter Channels (Hogg et al., 1999). The second transformation is the Vitória-Trindade Seamonts, which blocks and deflects the DWBC eastwards at latitude 20°S (Hogg and Owens, 1999).

1.3 Objectives

Mass transport across the Mid-Atlantic Ridge is crucial to understand the connection between the western and eastern basins of the South Atlantic and its role in the Atlantic Meridional Overturning Circulation. However, very few data have been collected in the depths of the ocean at the Mid-Atlantic Ridge. The South Atlantic Gateway (SAGA) project and this thesis aim to provide new measurements to study the exchanges between the water masses of the western and eastern basins of the ridge, to analyze the vertical structure of the deep layer and its temporal variability, as well as the influence of larger-scale phenomena on local circulation. In order to measure these water mass exchanges, the SAGA Array project was installed in March 2021 at 10°W (to the east of the ridge) between 19° S and 34°S at a depth of around 4000 m. This work focuses on the data collected by the furthest north mooring of the SAGA array (mooring 3).

2 Material and methods

Chapter Contents

2.1 Mooring measurements

The array consists of 5 pressure-equipped inverted echo sounders (PIES) separated by 5° and 3 moorings located between the PIES. A CTD measurement campaign named SAGA10W was simultaneously carried out on the same transect of the SAGA project (from 34°S to 19°S along 10°W) in order to quantify the exchanges between the basins through the MAR. To do this, the properties of the water masses were determined as well as the geostrophic circulation. The CTD stations were spaced 30 nautical miles apart.

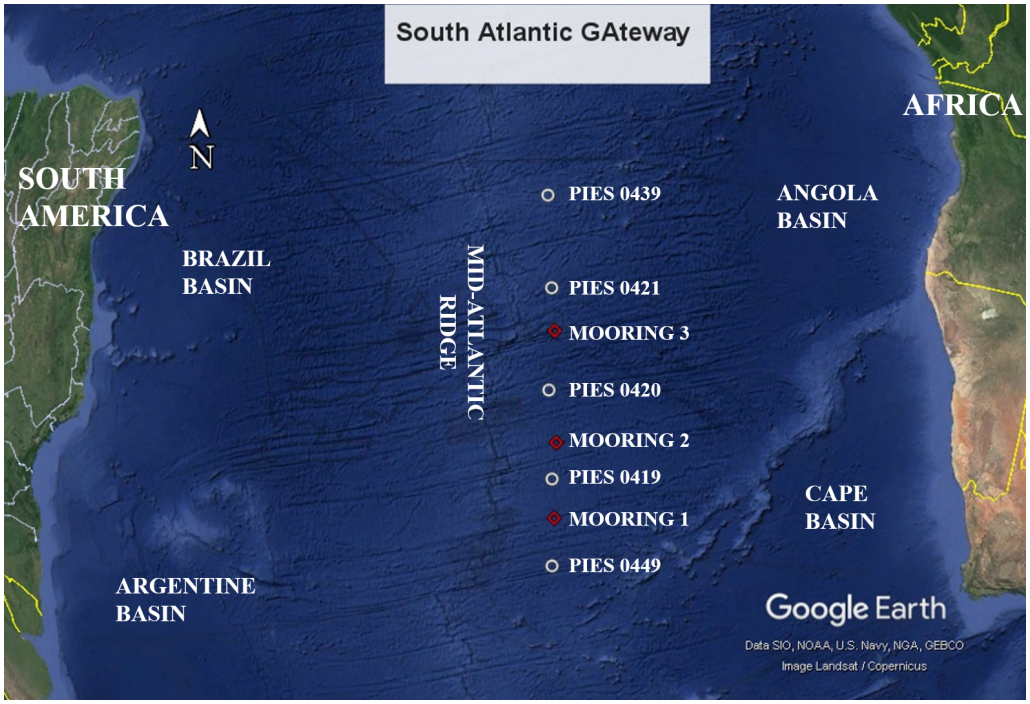

Figure 2.1: Map of the South Atlantic GAteway (SAGA) array indicating the location of instruments.

The mooring 3 whose data are studied in this work was installed on 31 March 2021 by the R/V *Sarmiento de Gamboa* (latitude: 21° 37.892‘ S, longitude: 09° 41.848’ W) and

recovered on 26 April 2023 during the SAGA Rec campaign by the *B.I.O Hespérides*. On arriving near the mooring deployment zone, a topography survey was carried out using a multibeam echosounder (MBES). The results of the topography survey and an illustration of the mooring are shown in Figure 2.2. Once the most suitable location had been chosen, a CTD measurement (ST033) was taken before installing the mooring. The mooring was fitted with 7 single-point recording current meters (RCM), 2 Sea-Bird MicroCat CTD sensors and 1 Workhorse Monitor 600kHz Acoustic Doppler Current Profiler (ADCP) from RD Instruments. The latter was not used for this work. The MicroCats were positioned above and below the mooring to measure temperature and salinity in order to identify the water mass in which the mooring has been installed. The various current meters are three Aanderaa SeaGuards (the data from one of them could not be used), three Nortek Aquadopps and one Aanderaa RCM 11. The data was collected in the NADW layer from 2351 m to 4407 m. Details of each instrument are shown in Table 2.1.

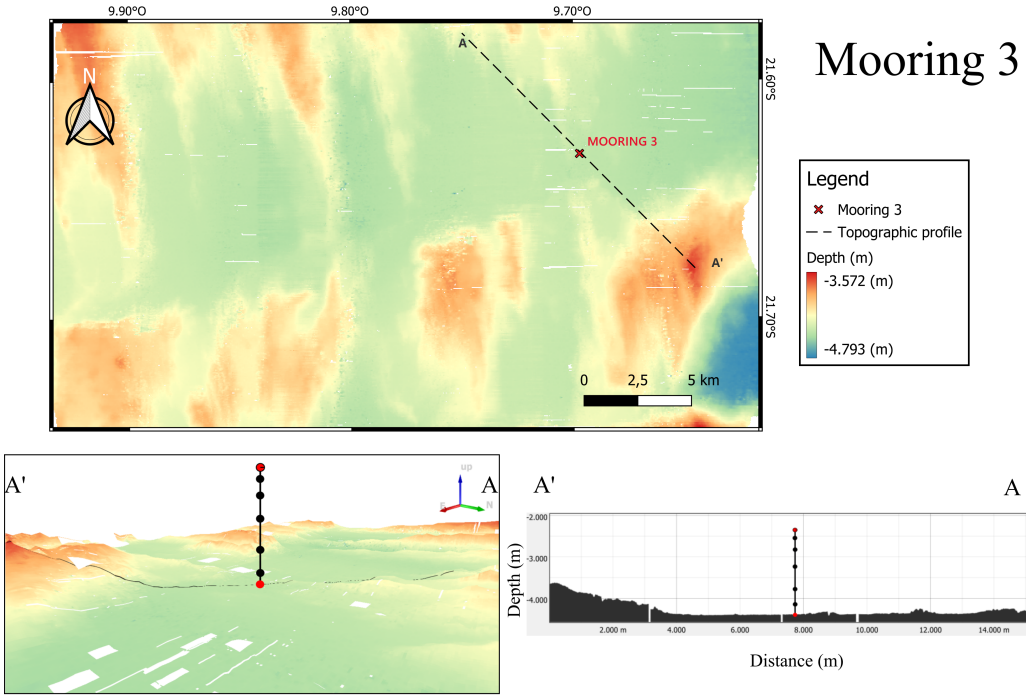

Figure 2.2: 2D and 3D map of the surrounding topography of the mooring. The topographical profile along the black dotted line is also shown. The position of the current meters on the mooring is indicated by black dots, while that of the MicroCats by red dots. The red dot edged in black indicates the presence of an Aanderaa SeaGuard and one of the two MicroCats at almost the same depth.

The measurements were filtered by a 36h Butterworth 6th-order low-pass filter to re-

Table 2.1: Instruments with their sampling details

Instruments	Depth (m)	Starting time	Interval	Ending time
Aanderaa Seaguard	2351	30 Mar 2021 21:00	1 hr	02 May 2023 09:00
Sea-Bird Microcat	2353	02 Apr 2021 20:00	1 hr	05 May 2023 19:00
Aanderaa RCM 11	2558	31 Mar 2021 22:30	1 hr	27 Mar 2023 01:12
Nortek Aquadopp	2843	01 Apr 2021 20:00	1 hr	30 Apr 2023 14:00
Aanderaa Seaguard	3249	30 MAr 2021 21:00	1 hr	01 May 2023 11:00
Nortek Aquadopp	3788	01 Apr 2021 20:00	1 hr	30 Apr 2023 17:00
Nortek Aquadopp	4191	01 Apr 2021 20:00	1 hr	30 Apr 2023 18:00
Sea-Bird Microcat	4407	31 Mar 2021 20:00	1 hr	05 May 2023 18:00

move tidal and inertial signals. In addition, a manual analysis was performed to remove outliers and data during the mooring launch and recovery, as indicated by a significant tilt of the instrument when measured. The accuracy of the instruments is presented in Table 2.2. In order to reduce the volume of data items and to ensure that they were synchronous, an interpolation of the daily data at 00:00 was performed using Matlab's interp1 function.

Table 2.2: Instrument's accuracy

Instruments	Conductivity	Temperature	Velocity
SBE37 MicroCat	± 0.003 mS/cm	± 0.002 °C	
Aanderaa Seaguard		± 0.03 °C	± 0.15 cm/s
Aanderaa RCM 11		± 0.05 °C	± 0.15 cm/s
Nortek Aquadopp		± 0.1 °C	± 0.5 cm/s

As the pressure was only measured by the SeaGuard located at the shallowest depth and the Aquadopps instruments (see Figure 2.1), the depth and pressure at which the other instruments are located was estimated using the length of the chain between the mooring instruments. In addition, as salinity (S) was only measured by the two MicroCats, the potential temperature (θ) could only be calculated at these two depths. However, the vertical temperature and salinity profiles from the campaigns carried out on the days when the mooring was launched and recovered allow the water masses to be recognised via a potential temperature-salinity diagram with neutral density (γ_n).

The vertical profiles of temperature and salinity also revealed a difference in the mea-

surements of salinity and temperature with those of the mooring at the first date when the measurement has been validated. The offsets in salinity between the MicroCats' measurements and those at their respective depths in the vertical profiles from the two campaigns were very similar. Thus the MicroCats time series were therefore corrected by removing the average of these offsets. Concerning the temperature differences between CTD and mooring measurements, the mooring instruments were 0.14°C-0.39°C higher than those of the first-day campaign, and only 0.002°C-0.014°C higher on the last day. This decrease in temperature difference is probably due to the adaptation time required for the mooring instruments. However, it's also possible that this offset was caused by a miscalibration of the CTD probe on the first day. As a result, the CTD measurements from the last day were used to determine the water mass.

For each current meter, mean current statistics were calculated as the mean and standard deviation of the north and east components of the current, the amplitude of the mean vector (SPD), and the stability of the current direction (STAB). The latter was evaluated by the ratio of the mean vector to the mean scalar speed (Dickson et al., 1985):

$$STAB = \frac{\sqrt{\left(\frac{1}{n}\sum_{i=1}^{N} u_i\right)^2 + \left(\frac{1}{n}\sum_{i=1}^{N} v_i\right)^2}}{\frac{1}{n}\sum_{i=1}^{N}\sqrt{u_i^2 + v_i^2}} \tag{2.1}$$

where u and v are the east and north components of the current respectively. The STAB parameter varies from 0 to 1 and increases when the current is stable in a certain direction.

The principal axes of the time series of the velocity vector of the various current meters were calculated. These principal axes form a new coordinate system in which the maximum variance is associated with the major axis and the minimum variance with the minor axis (Thomson and Emery, 2014). Thus the two axes differ by 90° and the principal angle θ_p ($\frac{-\pi}{2} \leq \theta_p \leq \frac{\pi}{2}$) is the angle between the east direction and that of the major axis (Freeland and Baker, 1975; Kundu and Allen, 1976; Preisendorfer, 1988). One technique for compressing data variability is to rotate the time series on its main axis. This method can also be useful for finding the main direction of the current at the depth of the current meter. In the case of this work, an angle was chosen for all the current meters, corresponding to the average of the 4 main angles of the 6 current meters studied. The two current meters not selected for averaging had significantly different principal angles. To further condense the information, ellipses whose half-axes correspond to the square root of the variance of the speed have been drawn and are oriented along the principal component axes.

To study the periodicity of the current time series, a frequency decomposition was carried out using a discrete fast Fourier Transform (fft) algorithm. To focus on large-scale phenomena, a 40-day low-pass filter was also applied to the data.

When calculating cross-correlation, 95% significance was calculated following Bendat and Piersol, 1980.

To calculate the westward propagation velocity of the Sea Level Anomaly (SLA) along the mooring longitude, the slope of the crest of the passage of the second SLA maximum shown in Figure 3.7 was used. This crest was chosen because it is the most pronounced over a long period of time, reducing the error introduced when choosing the two crest points for calculating the slope. The two points chosen from the Hovmöller diagram (Figure 3.7) are (October 28, 2021; -7.375°E) and (May 2, 2022; -16.125°E). The period between the two dates is then 186 days. The distance between the two points was calculated using a spherical approximation and the following equation:

$$\text{Distance} = R\cos(\text{latitude})\,\Delta\text{longitude} \tag{2.2}$$

where R is the Earth's radius, latitude is the latitude of the mooring and Δlongitude the difference between the two longitudes (in radians). The speed was then calculated by dividing this distance by the chosen period.

2.2 Other sources

For the calculation of the mean potential density over the years 1955-2022, temperature et salinity data from the World Ocean Atlas (WOA) data product of the Ocean Climate Laboratory of the National Centers for Environmental Information have been used (https://www.ncei.noaa.gov/access/world-ocean-atlas-2023/). The chosen grid is 1° wide, so the closest point to the mooring position is -21.5°N, -9.5°E.

Normal modes were calculated from the shallow-water m layered ocean model in 1 dimension. The layers are coupled by:

$$P = M^T D M\, h - b M^T D\, 1 \tag{2.3}$$

where P is the Montgomery potential, M is a m by m upper triangular matrix $M_{i,j} = 1$

for $i \leq j$ and zero otherwise, h is a vector of the thickness of each layer, b is the constant of bottom depth and D is a diagonal matrix whose non-zero elements are given by $D_{1,1} = g\rho_1$ and $D_{i,i} = g(\rho_{i+1} - \rho_i)$ for $i = 2, ..., m$. The second term of the equation being a constant, to decouple the m-layers model, eigenvectors (normal modes) and eigenvalues of the symmetric matrix $S = M^T DM$ are calculated.

Finally, a Hovmöller diagram of the Sea Level Anomaly (SLA) at 21.625°S from 31 March 2021 to 5 May 2023 is shown using satellite altimetry measurements from the Copernicus Climate Change Service (doi.org/10.48670/moi-00145). These anomalies are calculated daily with respect to the average height of the water surface over a reference period of 20 years (1993-2012). These data have been processed to Level 4, have a temporal resolution of 1 day and a spatial resolution of 0.25°x0.25°. The missions used are as follows : Topex/Poseidon between 1993-01-01 and 2002-04-23, Jason-1 between 2002-04-24 and 2008-10-18, Ocean Surface Topography Mission (OSTM)/Jason-2 between 2008-10-19 and 2016-06-25, Jason-3 between 2016-06-25 and 2022-02-09, and Sentinel-3 from 2022-02-10.

3 Results and discussion

Chapter Contents

3.1 Water masses analysis

Before studying the results of the data collected, it is important to know which water masses were measured. The water mass in which the mooring was installed is the NADW. Thanks to the CTD cast carried out on the day the mooring was recovered (26 April 2023), a potential temperature and salinity diagram was drawn (Figure 3.1). This CTD was used because it showed very small temperature differences with those measured by the mooring, unlike the CTD carried out on the day the mooring was launched. MicroCats placed at the ends of the mooring line deployment allow you to see in which water mass in the water column the mooring line is located. The salinity measured by the latter two was corrected as described in Chapter 2. The neutral density values displayed correspond to those delimiting the different South Atlantic water masses determined in Arumí-Planas et al., 2023 with the zonal hydrographic section of A095-24°S cruise at 24°S (Figure 3.2). The two MicroCats at 2353 m and 4407 m both measured temperature-salinity pairs on 26 April 2023 that correspond to the NADW characteristics described by Arumí-Planas et al., 2023, i.e. a potential temperature between 1.5°C and 2.5°C and a salinity between 34.85 and 34.9.

3.2 Mean flow statistics and principal component axes

In this section, we look at the time series of currents after the application of a 40-day low-pass filter. To summarise the information, Table 3.1 shows the calculated means and standard deviations of the eastern and northern components of the current. These values allow us to measure the importance of the temporal variability on the mean current at each depth measured. What can be observed is a large ratio of the standard deviation to the mean current at all depths signifying a preponderance of temporal variation over

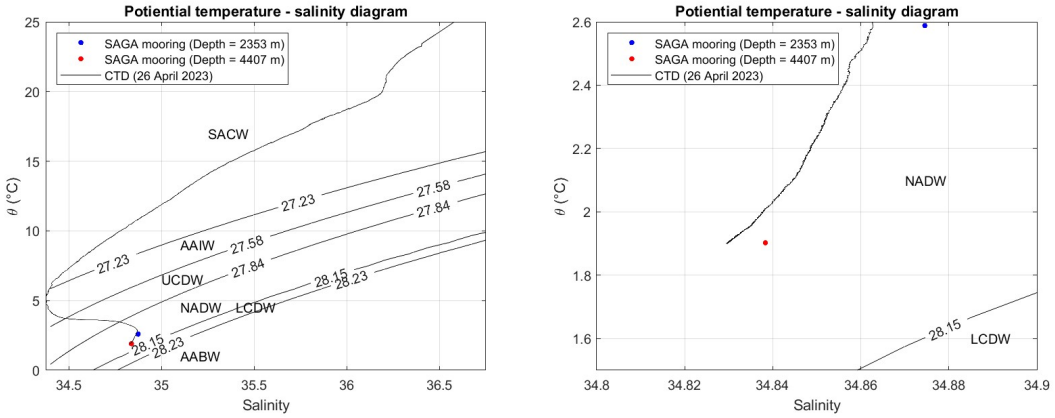

Figure 3.1: (a) Potential temperature-salinity (θ-S) diagram of the CTD carried out on the day the mooring was recovered. (b) A zoom on the depths where the MicroCats lie, between which the mooring extends. The isoneutral densities separating the different water masses are depicted. The water masses identified are: South Atlantic Central Water (SACW), Antarctic Intermediate Water (AAIW), Upper Circumpolar Deep Water (UCDW), North Atlantic Deep Water (NADW), Lower Circumpolar Deep Water (LCDW), and Antarctic Bottom Water (AABW).

mean current. The mean current speed (SPD) and stability of current direction (STAB) defined in Chapter 2 appear to increase with depth with the exception of a slight decrease at 3249 m. The higher SPD and STAB values for the two deepest current meters at 3788 m and 4191 m could be due to the influence of bathymetry around the mooring. Indeed, (see in Figure 2.2), these two current meters are located in a valley with a southwest-northeast direction.

This increase in current stability and strength with depth has already been observed in submarine canyons and valleys. Strongly oscillating currents in the canyon axis show a strong temporal correlation with semidiurnal tides, reaching often maxima between 25 and 50 cm/s (Shepard et al., 1979 Shanmugam, 2003). Berdeal et al., 2006 studied the vertical profile of currents in a 100 m deep, 1 km wide valley that divides the crest of the Juan de Fuca Ridge with a vertical resolution of 4 m. Their observations confirm the solution of their model and show that the sub-inertial components (period $>$ 16h for this latitude) of the current intensify and align with the valley axis towards the bottom. They explain this phenomenon by the weakening of the sub-inertial current perpendicular to the canyon axis with depth. This decrease in the component perpendicular to the canyon with depth leads to a decrease in the Coriolis force in the direction of the axis, which no longer fully compensates geostrophically for the pressure gradient force. This imbalance leads to an acceleration of the bottom current in the

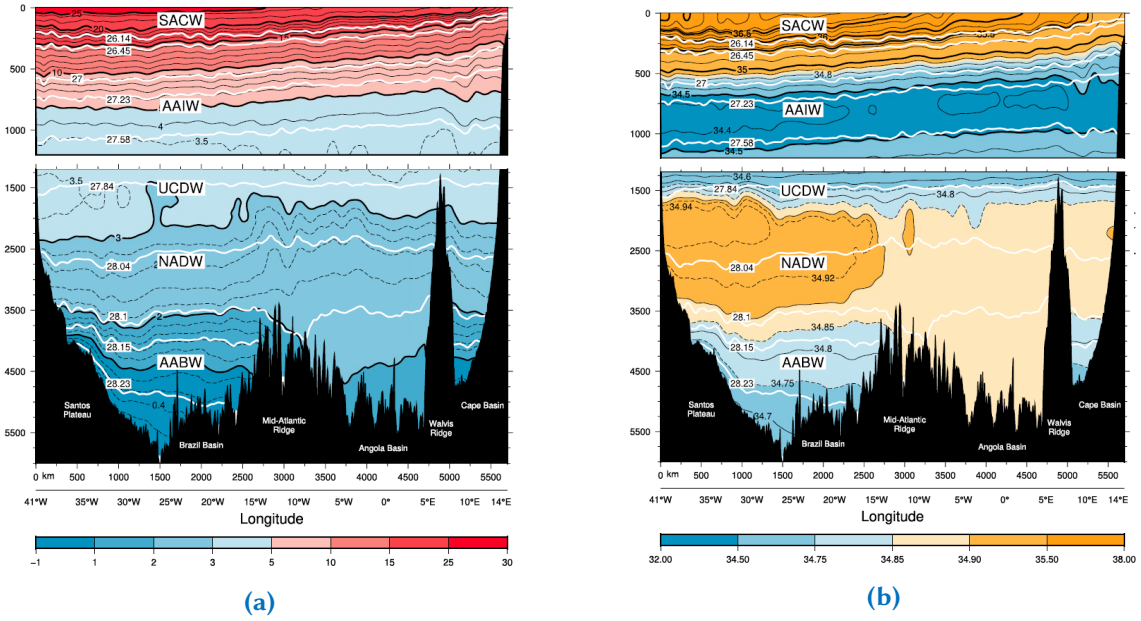

Figure 3.2: Vertical sections of (a) Atlantic Ocean (A09.5-24°S) - 2018 - θ (°C), (b) Atlantic Ocean (A095-24°S) - 2018 - salinity. The water masses identified are: South Atlantic Central Water (SACW), Antarctic Intermediate Water (AAIW), Upper Circumpolar Deep Water (UCDW), North Atlantic Deep Water (NADW), Lower Circumpolar Deep Water (LCDW), and Antarctic Bottom Water (AABW). The location of stations is indicated with the tick-marks on the top axis indicate the location of stations (Arumí-Planas et al., 2023).

direction of the canyon.

Although measurements of Berdeal et al., 2006 were brief (5 days) and might appear to be a passing event, longer measurements by Veirs, 2003 and Thomson et al., 2003 were carried out in the valley during the summers of 2000 and 2001 respectively, and also showed an mean current directed along the canyon axis and intensifying with depth. Thus, with SAGA mooring 3 located in the center of the valley, it seems that this increase in current stability and strength measured by the two deepest current meters can be explained in the same way, even after a 40-day low pass filtration. Moreover, erroneous instrument measurements appear to be less likely after checking the inclination of the instruments, which remains below the indicated threshold (20°) for reliable data. Even more reassuringly, processed data from SAGA's mooring 1 also show an increase in the stability and intensity of the mean current at the two deepest current meters (3788 m and 4001 m), also located in a valley (personal correspondence : Alberto Alcalá Verdugo (bachelor student)).

Table 3.1: Summary of mean flow statistics. SPD is the current mean speed, STAB is the ratio of the mean vector to the mean speed and indicates the directional stability.

Depth (m)	Days	SPD (cm/s)	STAB	East component (cm/s)	North component (cm/s)
2351	754	0.4	0.30	-0.4 ± 1.4	0.0 ± 0.7
2558	725	0.3	0.27	-0.1 ± 1.0	-0.3 ± 0.7
2843	754	0.8	0.41	0.0 ± 1.3	-0.7 ± 1.3
3249	755	0.5	0.32	0.4 ± 1.5	-0.2 ± 0.9
3788	754	0.9	0.46	0.8 ± 1.9	0.4 ± 0.9
4191	754	1.8	0.46	1.3 ± 3.0	1.2 ± 3.5

Having studied the stability and strength of the current as a function of depth, we can now turn our attention to its direction and whether we can compare it from the literature. In Table 3.1, the mean values for the east and north components of the current change sign with depth. This continuous variation in components reflects a mean current vector directed westwards over the top of the mooring, gradually turning southwards, eastwards and finally north-eastwards at 4191 m. This evolution from a mean westward current to a mean eastward current with depth is illustrated in Figure 3.3, which also shows the principal component axes, the daily velocities filtered by a 40-day low pass filter and ellipses whose half-axis lengths correspond to the square roots of the variances (standard deviations) along the principal component axes.

Although the shallowest current meter (2351 m) is located in the NADW layer, the mean westward current at the end of the two-year measurement period would correspond to the influence of the SEC, which carries water from the upper layers (AAIW and UCDW) northwestwards to the Brazilian coast. However, it should be noted that this mean current is very weak, due to its highly variable direction. Currents at this depth and at the next two current meters (2556 m and 2843 m) could be located in a transition layer between that influenced by the SEC and that dominated by the deep branch of the AMOC. In fact, the mean currents measured by the 3 deepest current meters (3249 m, 3788 m and 4191m) are directed eastwards. As mentioned in Section 1.2.2, the NADW leaves the Brazilian continental shelf when it encounters the Vitória-Trindade Ridge and turns eastwards, where part of it crosses the MAR between 20°S and 25°S (mooring latitude : 21° 37.892' S). It continues southwards via Cape Basin and follows the continental slope of South Africa (Larqué et al., 1997; Kersalé et al., 2019). This eastward mean current at the three deepest depths would then be due to the deep water transport from the Brazil Basin to the Angola Basin across the Mid-Atlantic Ridge.

To summarize the interpretation of the measured currents, the stability and strength of the current increases with depth, due to the presence of the valley in which the moor-

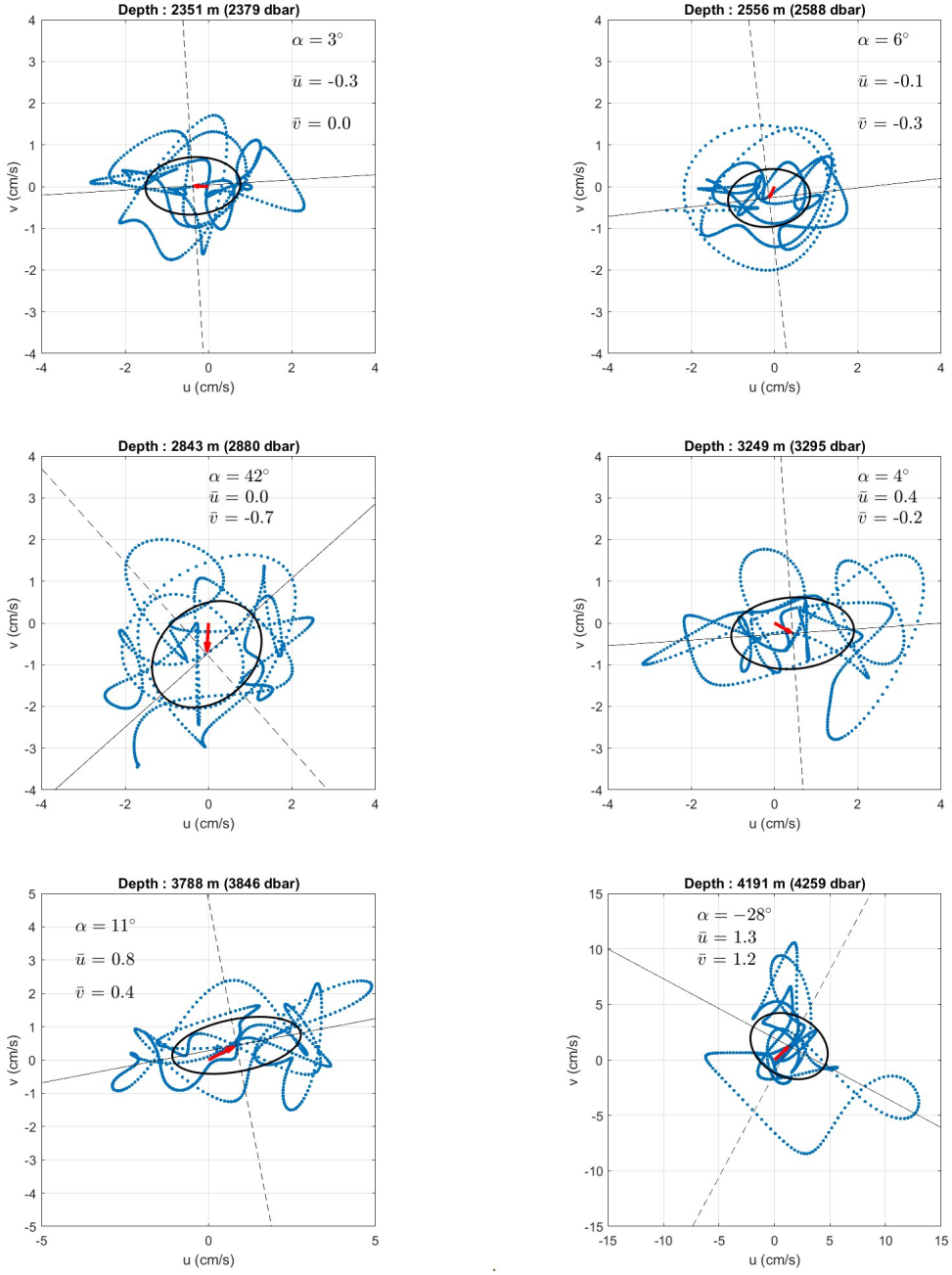

Figure 3.3: Principal component axes and the principal angle from the east α for the velocity from the current meters. The solid line indicates the major axis and the dashed line the minor axis. The red arrow is the mean vector and starts at (0,0) with its mean east component $\bar{u}$ and mean north component $\bar{v}$. The half-axes of the ellipses correspond to the square root of the variance of speeds measured along the main axes.

ing has been placed. The top of the mooring would still be slightly influenced by the SEC's westerly direction, while the bottom shows a mean current directed eastwards, as would be expected of part of the lower branch of the AMOC at these latitudes.

As explained in Chapter 2, the direction of the principal axes was calculated at each depth. By rotating the axes on this new coordinate system, current variability is compressed onto a single component, the major principal axis. The major principal axis along which the variance is greatest has an angle α between 3° and 11° with the east direction, with the exception of the current meters at 2843 m and 4191 m. These two meters showed an angle of 42° and -28° respectively. For the current meter at 2843 m, this could be explained by the greater dispersion of the current at this depth, making the calculation of the major axis more sensitive. In the case of the deepest current meter, a major event causing an intense southeasterly current could be responsible for this value of the major angle α. It's interesting to note that, with the exception of these last two current meters (2843 m and 4191 m), the major axis is generally zonally directed, meaning that the current oscillates more between west and east than between north and south. This result further confirms the presence of zonal water mass exchange (westward at the top of the mooring and eastward at the bottom).

3.3 Velocity component time series

As explained in Chapter 2, rotating the current time series on the main axes highlights its variation in the main current orientation. The east and north components of the current were thus rotated by a mean alpha angle of 6.2°. This mean angle does not take into account the principal angles obtained at 2843 m and 4191 m, as their values differ greatly from the others. Figures 3.4 and 3.5 show the time series of current meters along the major and minor main axes respectively, throughout the mooring period.

The time series in Figure 3.4 shows that the current varies similarly throughout the water column, with the exception of the deepest current meter at 4191 m. Indeed, the cross-correlations of each time series with that of the lower depth show maximum values of 0.77 to 0.86, while the cross-correlation between the time series of the two greater depths (3788 m and 4191 m) shows a maximum value of 0.32. The variations between positive and negative values reflect relatively simultaneous alternations between eastward and westward currents over the entire NADW depth measured. Current oscillations are more frequent for the 3 upper current meters (at 2351 m, 2556 m and 2843 m) than for the deeper ones, where the current is on average more eastwardly directed, as

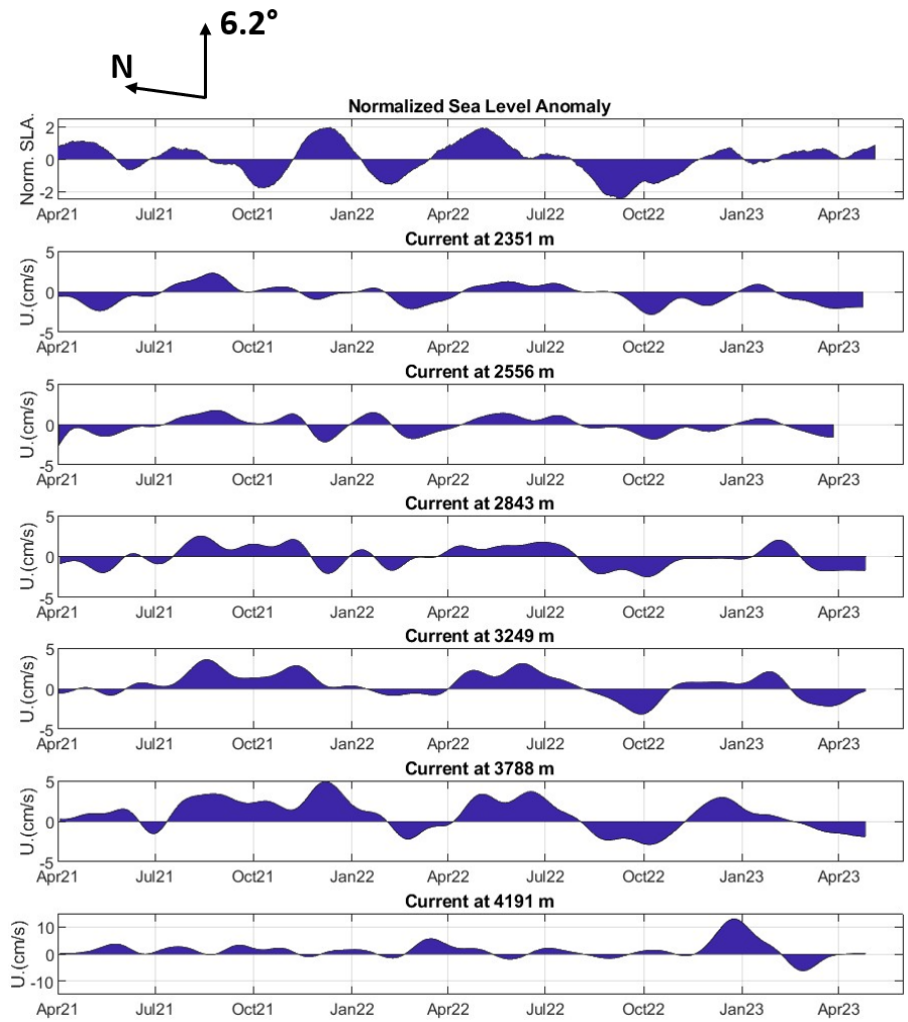

Figure 3.4: Time series of the normalized sea level anomalies and of the major principal component of 40-day low-pass currents. Note: the scale is different for the time series of the last current meter, for better legibility.

observed by the mean vectors in Figure 3.3. As previously observed, the current intensifies with depth.

The velocity component in the direction of the minor principal axis (Figure 3.5) also shows simultaneity in its variations throughout the water layer measured, with the exception of the deepest current meter at 4191 m. The cross-correlations between each successive series show maximum values of 0.51 to 0.79, while the cross-correlation between the two deepest time series (3788 m and 4191 m) shows a maximum value of 0.25. Note that at this depth, the current component measured along the minor principal axis also reaches significant values of up to 10 cm/s between April and May 2022. As expected from the choice of projecting the components along the principal axes along

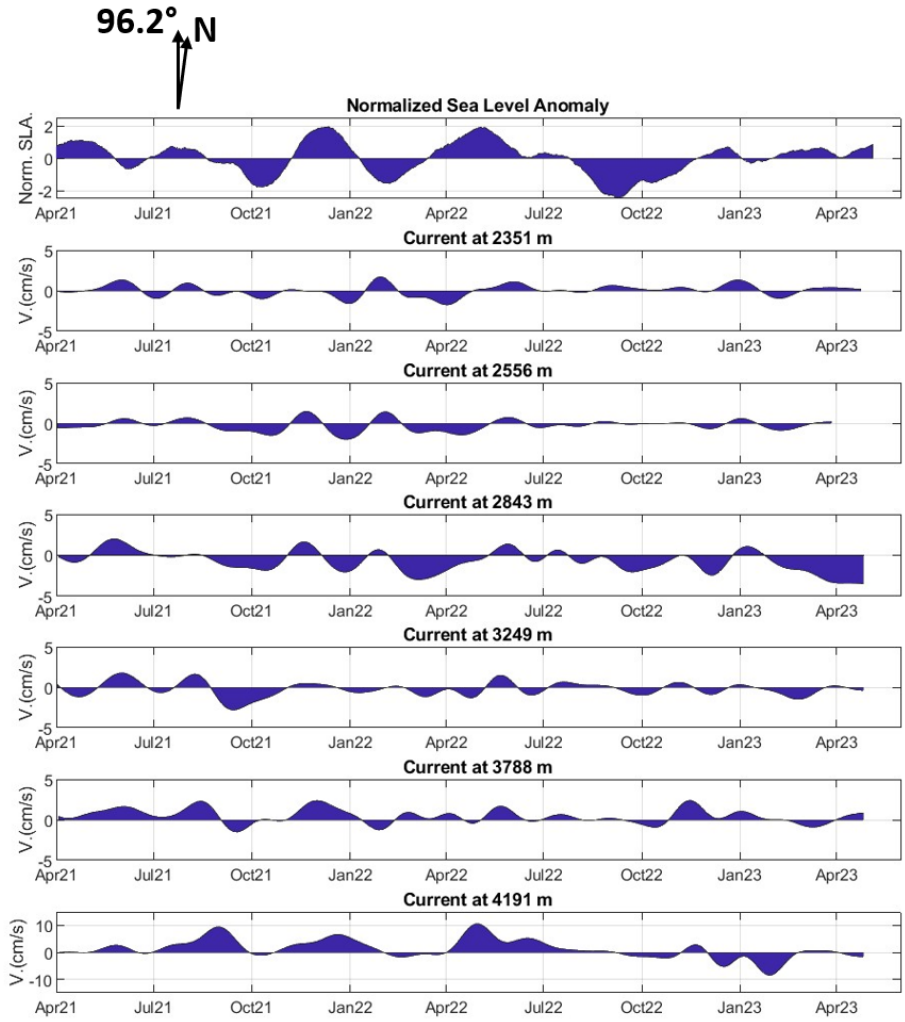

Figure 3.5: Time series of the normalized sea level anomalies and of the minor principal component of 40-day low-pass currents. Note: the scale is different for the time series of the last current meter, for better legibility.

which the squares of the normal distances to the data points are extreme (Thomson and Emery, 2014), the current oscillates between lower values along the minor principal axis (Figure 3.5) than along the major principal axis (Figure 3.4). However, the amplitude of oscillation is similar between the two components at depths of 2843 m and 4191 m, where the calculated principal angle is significantly different from 6.2°.

3.4 Fourier analysis

To investigate whether there are any periodic phenomena in the measured currents, a Fourier analysis of the time series of each current meter was performed. As the data

did not contain any gaps, a Fast Fourier Transform algorithm was used to calculate the discrete Fourier Transform and extract the harmonics (Li, 2022). As the measurement period lasts only 2 years, only seasonal or even annual variations can be detected.

Table 3.2 shows the frequencies contained in the time series of velocity component perturbations along the major principal axis. To remove the zero-frequency peak, the mean has been removed from each original signal. The strongest signal is an 8-month period for all depths except 3788 m, where it is 6 months. This difference could be due to the finite and discrete nature of the data time series, which implies a low resolution of peak position for periods approaching the measured period length. The main peaks (8 months or 6 months, depending on the current meter) show a much greater amplitude than the secondary peaks, with the exception of the deepest current at 4191 m, where 3 peaks of similar amplitude stand out at 8, 5 and 3 months. This suggests that the current at this depth is influenced by other phenomena than that which predominates over the entire measured layer.

Table 3.2: Frequencies contained in the time series of velocity components along the major principal axis.

Current Meter Depth (m)	Frequency months (days)	Amplitude (cm/s)
2351	8 (251)	0.9
2351	4 (126)	0.5
2558	8 (242)	0.7
2558	3 (91)	0.5
2843	8 (251)	1.3
2843	2 (75)	0.5
3249	8 (252)	1.3
3249	2 (75)	0.5
3788	6 (189)	1.6
3788	4 (126)	0.7
4191	8 (251)	1.9
4191	5 (151)	1.8
4191	3 (94)	1.7

3.5 Interpolation of vertical current profiles

To better visualize the temporal evolution of current and temperature throughout the measured water layer, an interpolation was made using the DIVA (Data-Interpolating Variational Analysis) gridding method (Barth et al., 2010) as implemented in Ocean DataView. Figure 3.6 shows the interpolated vertical profile of the east and north components of current and temperature. The parameters for the DIVA gridding have been fixed to 100 permille and 300 permille for the horizontal and vertical axis respectively and the signal-to-noise ratio to 30.

Figure 3.6a shows that in-situ temperature oscillations occur over the entire measured water column and throughout the mooring period. During the 2 years of measurement and at all depths, several events lasting around 2 months are visible, during which warmer water reaches greater depths. For some of these events, the temperature increase is almost simultaneous at all depths, while for others, the temperature begins to rise chronologically at the deepest instruments. In all, 4 events were observed.

Based on Figure 3.6, it is easier to observe the vertical coherence of the eastern and northern components of the current. As with temperature, current fluctuations occur almost simultaneously at the depth of all current meters. There are 4 major events during which the eastern component of the current increases. Interestingly, these increases in the eastern component of the current all took place shortly after the warmer waters began to sink to depth. The cross-correlation between the eastern components of the current and temperatures measured at the same depths (2351 m, 2556 m and 4191 m) shows a maximum at a lag of around 30 days within a 95% confidence interval of significance. Cross-correlation maxima at depths of 2843 m and 3788 m did not show sufficient confidence. This suggests these temperature rises events precede eastward current strength increase events by around 1 month.

We can also note that the cross-correlation between the evolution of the eastern component of the current meter at 2351 m and that of salinity measured by the Microcat at 2353 m shows a significant correlation maximum at 28 days. Thus, as with temperature, increases in salinity precede increases in the eastern component at this depth by around 1 month. This result is consistent with the descent of higher water to lower depths leading to higher temperature and salinity. The potential temperature-salinity diagram in Figure 3.1b also showed a tendency for temperature and salinity to decrease with depth. The time series of salinity measured by the Microcat at 4407 m

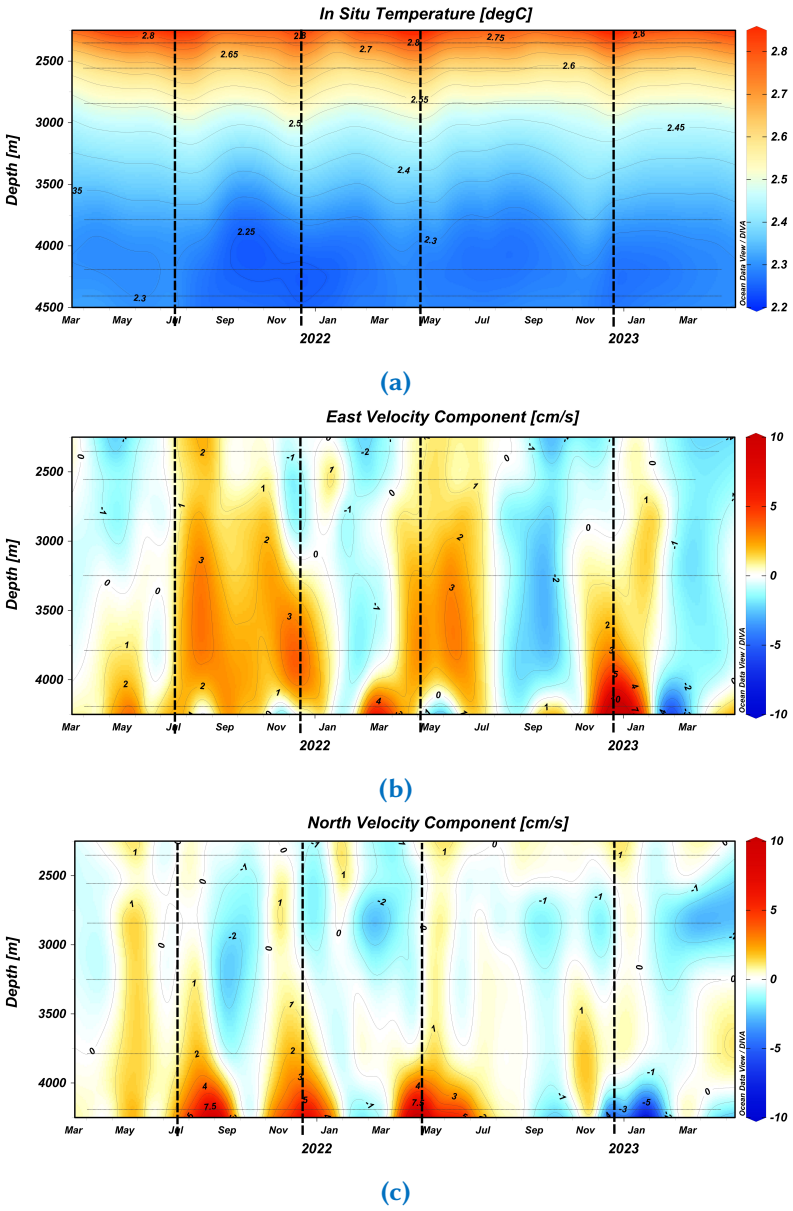

Figure 3.6: Vertical profiles of (a) in-situ temperature and of (b) the east and (c) north components of the current, produced by interpolation using the DIVA (Data-Interpolating Variational Analysis) gridding method (Barth et al., 2010) as implemented in Ocean DataView. Points forming horizontal lines are daily data. The vertical dotted lines indicate the dates on which maximum sea level anomalies above the mooring were measured, as explained in greater detail in Chapter 3.6.

was not studied through cross-correlation due to the lack of current measurements at nearby depths.

As for the link between variations in the northern component of the current and temperature, none of the cross-correlation calculations showed a correlation maximum within the confidence interval, with the exception of Aquadopp at 3788 m depth, which showed a significant maximum at a lag of -4 days. It would seem that, unlike the eastern component of the current, variations in the northern component do not clearly correlate with those in temperature over the entire depth measured.

Once these links had been established, an explanation was sought for the correlation between the eastern component of the current and temperature fluctuations. The idea that a mass of warmer, saltier water is being carried eastwards by increases in the eastern component of the current was considered. However, it is the temperature increases that precede those of the current's eastern component, not the other way round. In fact, a current would have to intensify sufficiently and for a sufficiently long time to displace a mass of water with slightly different characteristics and to observe variations at the mooring point.

However, although temperature variations are globally synchronous along depth, it is interesting to note a certain time lag at the last rise (November-December 2022). Indeed, the temperature maximum at 4191 m depth occurs on November 4, 2022, while at 2351 m, the maximum occurs on December 12, 2022. This gradual shift in temperature increase is also associated with a particular event, as it can be seen from Figure 3.6b that the increase in the eastern component of the current is not present throughout the entire measured water column. In fact, the increase in the eastern component of the current is significant between 3240 m and 4191 m, whereas it is absent in the upper layers. An earlier increase in temperature at greater depths, where the eastward component is strongest, suggests the possibility of a horizontal influx of slightly warmer water. Salinity measurements at these depths could have helped to better identify the characteristics of this water coming from the west.

3.6 Influence of Rossby waves on current variability

This previous result motivated the search for Rossby waves during the period measured and in the search zone. Indeed, Hernández-Guerra and Talley, 2016 and Arumí-Planas et

al., 2022 had already observed quasi-barotropic disturbances of the current down to the ocean floor during the passage of long baroclinic Rossby waves along a hydrographic transect at 32°S in the Pacific Ocean.

As proposed by Cipollini et al., 1998, Sea Level Anomalies (SLA) at the latitude closest (21.625°S) to that of the mooring (21.631°S) and along time were examined to detect the passage of Rossby waves, relying on the zonal propagation of those waves. A Hovmöller diagram (Figure 3.7) was then drawn using satellite altimetry data provided by the Copernicus Climate Change Service (see Chapter 2), corresponding to the mooring period. On the diagram, sea level disturbances with an amplitude of 0.1 m to 0.2 m propagate westwards, as observed by Hernández-Guerra and Talley, 2016 and Arumí-Planas et al., 2022 at 32°S in the Pacific Ocean. The central vertical line indicates the position of the mooring (9.697° W) on the longitude axis. The horizontal dotted lines indicate the maximum anomalies dates and are considered to be the moment the Rossby wave passes over the mooring. Four dates have been identified.

Thanks to the slope of the second anomaly crest (crossing the mooring in december 2021) shown in Figure 3.7, a zonal propagation velocity of 4.86 km/day (5.6 cm/s) towards the west was calculated (see Chapter 2 for details). This result corresponds very well to the estimate of Rossby wave propagation speed as a function of latitude (about 5.5 km/day) obtained by Cipollini et al., 1998 using the Fast Fourier Transform of a Hovmöller diagram, which is also in good agreement with the predictions of Rossby wave theory (Killworth et al., 1997). Thus, the sea level anomaly propagations observed above the mooring propagate well at the speed of long baroclinic Rossby waves.

Satellite data of Sea Level Anomalies have made it possible to detect the dates of passage of the various Rossby waves over the mooring, but they do not allow us to determine their vertical structure. Indeed, to understand the consequences on the vertical profile of temperature and currents, it may be useful to calculate the vertical structure of the various normal modes of the water layer studied. To this end, time averages (1955-2022) of the temperature and salinity of the entire water column at the coordinate closest to the mooring (21.5°S; 9.5°W) were required, provided by the World Ocean Atlas of the National Centers for Environmental Information. The various normal modes were then calculated from the deduced vertical profile of potential density as explained in Chapter 2. These modes are shown in Figure 3.8. The pink area indicates the part of the water column occupied by the mooring. In this area, the various modes are constant at non-zero values, although the barotropic mode predominates. This is consistent with

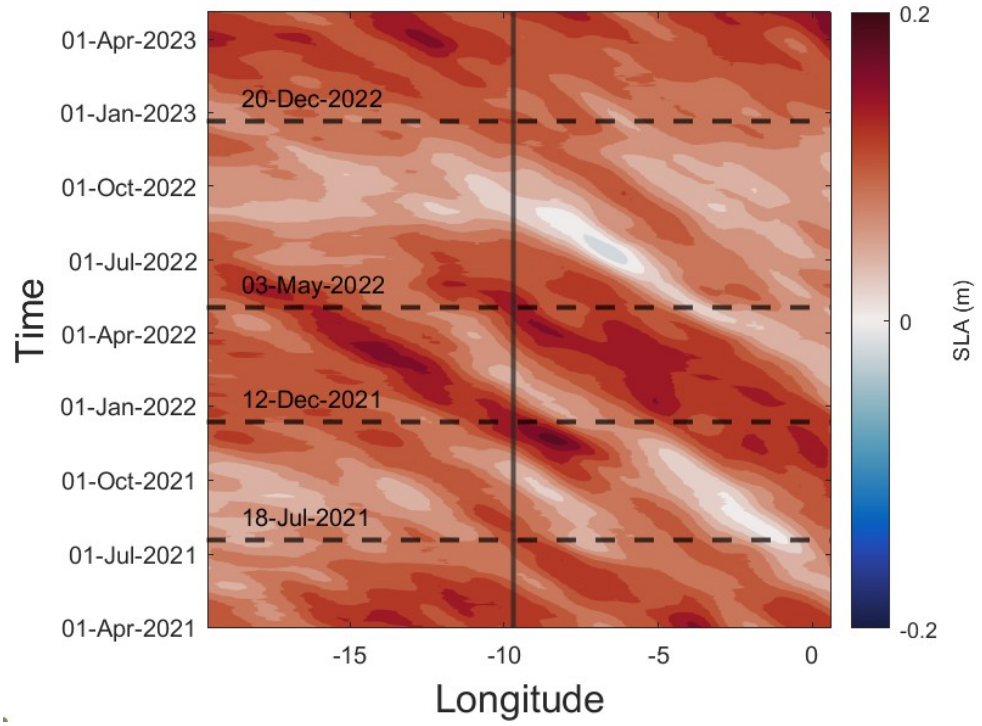

Figure 3.7: Sea Level Anomaly (m) along 21.625°S in the Atlantic Ocean from April 2021 to April 2023. The vertical line indicates the mooring's longitude (9.697° W). The horizontal dotted lines indicate the dates on which maximum sea level anomalies above the mooring were measured. Satellite altimetry measurements from the Copernicus Climate Change Service (doi.org/10.48670/moi-00145). See Chapter 2 for more details.

the fact that density varies very little from the top to the bottom of the mooring. Indeed, temperature and salinity vary little at mooring depth, as shown in Figure 3.1. This also explains why temperature and current vary mainly synchronously over the entire measured depth. These observations are in line with those made by Arumí-Planas et al., 2022, who also observed sea surface anomalies propagating westwards at a speed of 3 cm/s at 32°S in the Pacific Ocean, associated with quasi-barotropic disturbances in the circulation down to the ocean bottom.

Now we can understand why measured temperature increases occur almost simultaneously at all depths and at the same time as Sea Level Anomalies (see 3.9). The dotted vertical lines indicating the maximum of SLA of each Rossby wave passage on the Hovmöller diagram (Figure 3.7) have been transposed onto the time series of temperature and velocity components in Figure 3.6. It can thus be seen that the passage of a Rossby wave immediately leads to an increase in temperature throughout the water column. These rises in the ocean surface are due to the convergence of water at the

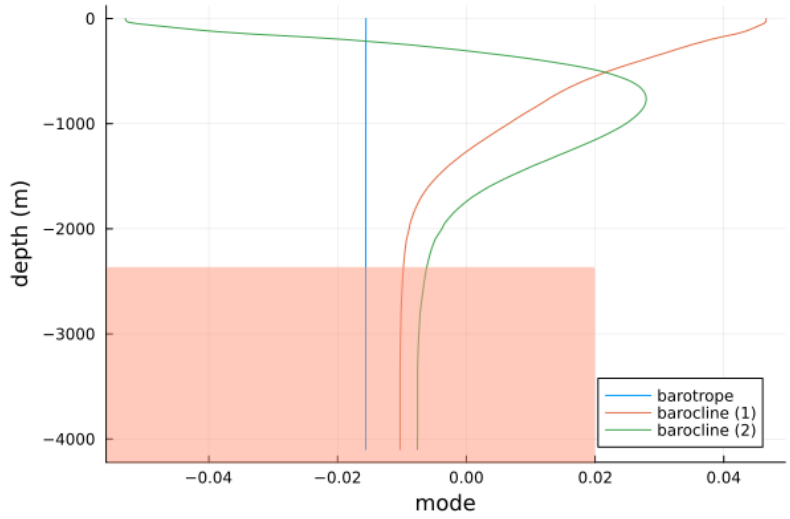

Figure 3.8: Vertical structure of the barotropic mode and first and second baroclinic modes calculated thanks time average (1955-2022) of the temperature and salinity of the entire water column at the closest coordinate to the mooring (21°5S; 9.5°W). The pink area indicates the part of the water column occupied by the mooring. Data from the World Ocean Atlas (WOA) data product of the Ocean Climate Laboratory of the National Centers for Environmental Information (https://www.ncei.noaa.gov/access/world-ocean-atlas-2023/).

center of the anticyclonic circulation associated to the Rossby wave, driven by Ekman transport. This accumulation of water at the center of the Rossby wave perturbation in turn causes the water to sink to the bottom, dragging the isotherms with it. Instruments fixed at a constant depth measure then an increase in temperature, followed by cooling as the wave passes.

Variations in current components could be explained by looking at the passage of the mooring position through the pattern of circulation disturbances created by the Rossby wave. For sea-level rises, this pattern corresponds to anticyclonic circulation, as explained above. So, given that Rossby waves propagate mainly zonally, the passage of the Rossby wave over the mooring should generate an oscillation in the northerly component of the current. Thus, the arrival of the Rossby wave should contribute to a more southerly current, given that the mooring in question is in the southern hemisphere. On the contrary, when the anomaly maximum passes over the mooring and the Rossby wave moves away, this should contribute to a more northerly current. This line of reasoning could be applied to Figure 3.6c, where the northern component of the current appears to change sign as it passes the maximum sea level anomaly indicated by the vertical dotted lines.

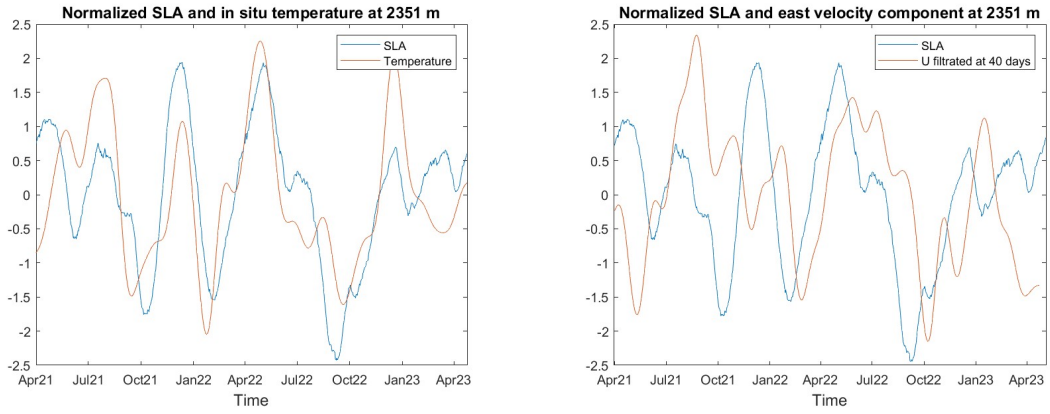

(a) (b)

Figure 3.9: Normalized Sea Level Anomaly (SLA) over the mooring with (a) normalized in-situ temperature and (b) normalized east velocity component at 2351 m.

With the passage of the second Rossby wave in December 2021, however, the northern component of the current changes from positive (northward) to negative (southward) values. Indeed, it is important to keep in mind that measured currents are relatively deep and are compared to variations in ocean surface height. In addition, there is also a mean circulation that adds to the disturbances caused by the passage of the Rossby wave. As a result, the simple model presented here may not always match observations.

Following strictly the same reasoning as for the northern component of the current, the eastern component of the current should not be affected by the passage of the Rossby wave if its center passes over the mooring. However, the propagation speed of the Rossby wave also has a meridional (northward) component, and it is also possible that the disturbance pattern is not centered on the mooring when crossing it (see Figure 3.10). Thus, the effect of the passage of the Rossby wave on the eastern component of the current is also significant, although more variable depending on the trajectory of the Rossby wave relative to the position of the mooring. Indeed, in Figure 3.9, the normalized SLA signal and the signal of the eastward component of the current at 2351 m are quite similar, with a lag of approximately 1 month. In Figure 3.6b, the eastern component of the current also changes sign with the passage of the first Rossby wave in July 2021, shifting from a westerly to an easterly current. As can be observed for other Rossby waves, its passage has different effects on the eastern component of the current, probably due to whether the wave passes to the north or south of the mooring. As shown in Figure 3.11, on May 3, 2022, a day when a maximum SLA was recorded above the mooring, the center of the Rossby wave (where the maximum sea level anomaly is

located) passed directly over the mooring. However, on December 20, 2022, during another maximum SLA recorded above the mooring, the center of the Rossby wave passed to the south of the mooring. One way of understanding these phenomena on a case-by-case basis would be to track the displacement of Rossby waves via SLA maps according to longitude and latitude and the surface current velocity field.

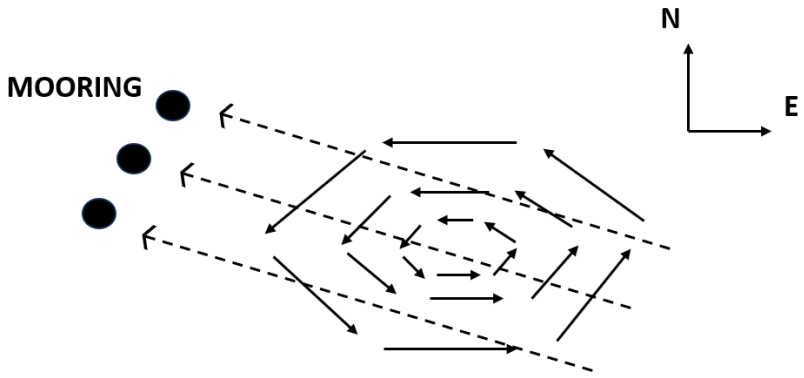

Figure 3.10: Drawing representing the different trajectories (dotted arrows) that Rossby wave perturbations can take relative to the position of the mooring (black dots), with the anticyclonic circulation associated with the Rossby wave symbolized by solid arrows.

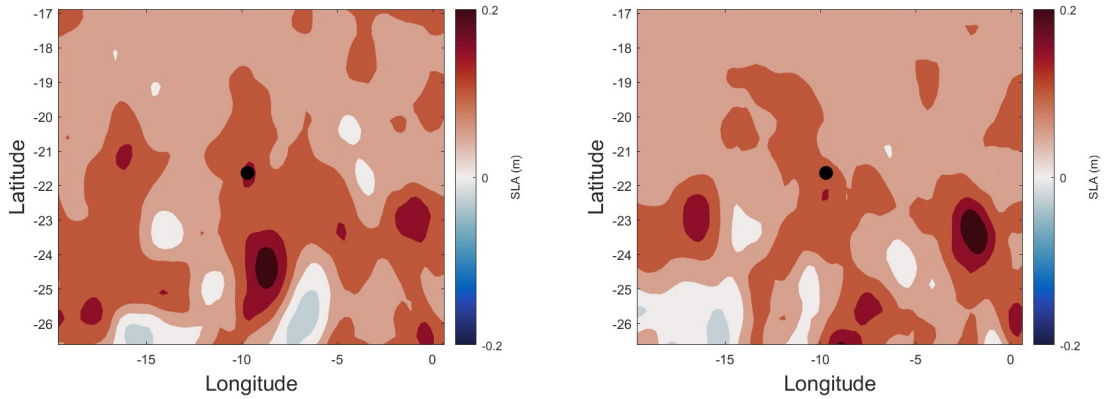

Figure 3.11: Sea level anomaly (SLA) around the mooring (black dot) on (a) May 3, 2022, and (b) December 20, 2022, when SLA maxima were recorded above the mooring.

4 Conclusion and perspectives

Chapter Contents

4.1 Conclusion

This thesis focused on the processing and analysis of data from a mooring that is part of the larger SAGA project. Positioned between 2351 m and the ocean floor at 4407 m, this mooring was able to measure currents, temperature, and salinity for nearly two years between April 2021 and April 2023 on the eastern edge of the Mid-Ocean Ridge in the South Atlantic Ocean.

Firstly, the water mass in which the mooring was placed was identified as the NADW thanks to the water mass characteristics at this latitude provided by Arumí-Planas et al., 2023 and in accordance with the studies of Larqué et al., 1997 and Talley, 2011.

The study of currents showed the predominance of current variability over the mean current at all depths. Moreover, an increase in current intensity and stability with depth was measured, as has been observed in other canyons and submarine valleys (Shepard et al., 1979; Shanmugam, 2003; Berdeal et al., 2006), and was therefore attributed to the influence of bathymetry on the mean current.

The average current direction also aligns with the descriptions by Larqué et al., 1997 and Kersalé et al., 2019. Although located within the NADW water mass, the current meters situated in its upper part (2351 m, 2556 m) showed a weak westward mean current, suggesting the influence of the overlying South Equatorial Current, while the deeper current meters showed an eastward mean current corresponding to the transport of NADW from the Brazil Basin to the Angola Basin across the Mid-Ocean Ridge at these latitudes.

Finally, temperature and current disturbances were compared with sea level anomalies and identified as those caused by the passage of long baroclinic Rossby waves. These observations are similar to the quasi-barotropic current perturbations observed by Hernández-Guerra and Talley, 2016 and Arumí-Planas et al., 2022 down to the ocean

floor at 32°S in the Pacific Ocean during the passage of long baroclinic Rossby waves.

4.2 Perspectives

During the analysis of water masses and currents, the lack of salinity measurements was a significant shortcoming. It would have been useful, for instance, to know the salinity and potential temperature at different depths to investigate whether horizontal transport of water with different characteristics occurred during the large increases in the eastward component of the current. Then, it would be beneficial to incorporate more sensors capable of measuring salinity to calculate potential temperature, as well as some that can measure oxygen concentration along the entire cable. This would enable a better identification of the different water masses that the mooring traverses. A deployment lasting longer than two years would also allow for the detection of interannual variability and provide a more detailed study of the presence of signals with seasonal or annual variability.

The study of currents along the mooring revealed that bottom currents were strongly influenced by bathymetry. Although already studied in canyons and submarine valleys around the world, little is known about bottom currents above the Mid-Atlantic Ridge. Further study using moorings with better vertical resolution at depths influenced by bathymetry would provide a better understanding of bottom current mechanisms and their importance in communication between the western and eastern basins of the South Atlantic Ocean and in the AMOC.

In addition, the study of the influence of Rossby waves on current variation could be pursued by simultaneously comparing Rossby wave tracking via latitude-longitude maps of sea level anomalies, surface currents and vertical profiles of currents and temperatures measured by moorings. This data set would potentially enable the development of a simple model to explain the vertical profiles of current variations as a function of the Rossby wave's path relative to the mooring's position.

Finally, this thesis should be compared with the results of the rest of the SAGA project in order to gain a better understanding of the two previous points mentioned above and, more importantly, a broader understanding of the role of water mass transport over the Mid-Atlantic Ridge in the AMOC.

Bibliography

Arumí-Planas, C., Hernández-Guerra, A., Caínzos, V., Vélez-Belchí, P., Farneti, R., Mazloff, M. R., Mecking, S., Rosso, I., Chretien, L. M. S., Speer, K. G., et al. (2022). Variability in the meridional overturning circulation at 32 s in the pacific ocean diagnosed by inverse box models. *Progress in Oceanography*, *203*, 102780.

Arumí-Planas, C., Pérez-Hernández, M. D., Pelegrí, J. L., Vélez-Belchí, P., Emelianov, M., Caínzos, V., Cana, L., Firing, Y. L., García-Weil, L., Santana-Toscano, D., et al. (2023). The south atlantic circulation between 34.5° s, 24° s and above the mid-atlantic ridge from an inverse box model. *Journal of Geophysical Research: Oceans*, *128*(5), e2022JC019614.

Barth, A., Alvera-Azcárate, A., Troupin, C., Ouberdous, M., & Beckers, J.-M. (2010). A web interface for griding arbitrarily distributed in situ data based on data-interpolating variational analysis (diva). *Advances in Geosciences*, *28*, 29–37.

Beal, L. M., De Ruijter, W. P., Biastoch, A., & Zahn, R. (2011). On the role of the agulhas system in ocean circulation and climate. *Nature*, *472*(7344), 429–436.

Bendat, J. S., & Piersol, A. G. (1980). Engineering applications of correlation and spectral analysis. *New York*.

Berdeal, I. G., Hautala, S. L., Thomas, L. N., & Johnson, H. P. (2006). Vertical structure of time-dependent currents in a mid-ocean ridge axial valley. *Deep Sea Research Part I: Oceanographic Research Papers*, *53*(2), 367–386.

Biastoch, A., Böning, C. W., & Lutjeharms, J. (2008). Agulhas leakage dynamics affects decadal variability in atlantic overturning circulation. *Nature*, *456*(7221), 489–492.

Boebel, O., Davis, R., Ollitrault, M., Peterson, R., Richardson, P., Schmid, C., & Zenk, W. (1999). The intermediate depth circulation of the western south atlantic. *Geophysical Research Letters*, *26*(21), 3329–3332.

Broecker, W. S., Sutherland, S., & Peng, T.-H. (1999). A possible 20th-century slowdown of southern ocean deep water formation. *Science*, *286*(5442), 1132–1135.

Buscaglia, J. L. (1971). On the circulation of the intermediate water in the southwestern atlantic ocean.

Caesar, L., Rahmstorf, S., Robinson, A., Feulner, G., & Saba, V. (2018). Observed fingerprint of a weakening atlantic ocean overturning circulation. *Nature*, *556*(7700), 191–196.

Caínzos, V., Hernández-Guerra, A., McCarthy, G., McDonagh, E. L., Cubas Armas, M., & Pérez-Hernández, M. D. (2022). Thirty years of goship and woce data: Atlantic overturning of mass, heat, and freshwater transport. *Geophysical Research Letters*, *49*(4), e2021GL096527.

Cipollini, P., Cromwell, D., & Quartly, G. (1998). Observations of rossby wave propagation in the northeast atlantic with topex/poseidon altimetry. *Advances in Space Research*, *22*(11), 1553–1556.

Cunningham, S. A., Kanzow, T., Rayner, D., Baringer, M. O., Johns, W. E., Marotzke, J., Longworth, H. R., Grant, E. M., Hirschi, J. J.-M., Beal, L. M., et al. (2007). Temporal variability of the atlantic meridional overturning circulation at 26.5 n. *science*, *317*(5840), 935–938.

Desbruyères, D. G., Mercier, H., Maze, G., & Daniault, N. (2019). Surface predictor of overturning circulation and heat content change in the subpolar north atlantic. *Ocean Science*, *15*(3), 809–817.

Dickson, R., Gould, W., Müller, T. J., & Maillard, C. (1985). Estimates of the mean circulation in the deep (¿ 2,000 m) layer of the eastern north atlantic. *Progress in Oceanography*, *14*, 103–127.

Evans, D. L., & Signorini, S. S. (1985). Vertical structure of the brazil current. *Nature*, *315*(6014), 48–50.

Frajka-Williams, E., Ansorge, I. J., Baehr, J., Bryden, H. L., Chidichimo, M. P., Cunningham, S. A., Danabasoglu, G., Dong, S., Donohue, K. A., Elipot, S., et al. (2019). Atlantic meridional overturning circulation: Observed transport and variability. *Frontiers in Marine Science*, *6*, 260.

Freeland, J. R., & Baker, N. R. (1975). Goal partitioning in a hierarchical organization. *Omega*, *3*(6), 673–688.

Fu, Y., Li, F., Karstensen, J., & Wang, C. (2020). A stable atlantic meridional overturning circulation in a changing north atlantic ocean since the 1990s. *Science Advances*, *6*(48), eabc7836.

Ganachaud, A. (2003). Large-scale mass transports, water mass formation, and diffusivities estimated from world ocean circulation experiment (woce) hydrographic data. *Journal of Geophysical Research: Oceans*, *108*(C7).

Ganachaud, A., & Wunsch, C. (2000). Improved estimates of global ocean circulation, heat transport and mixing from hydrographic data. *Nature*, *408*(6811), 453–457.

Garzoli, S. L., & Matano, R. (2011). The south atlantic and the atlantic meridional overturning circulation. *Deep Sea Research Part II: Topical Studies in Oceanography*, *58*(17-18), 1837–1847.

Gordon, A. L. (2003). The brawniest retroflection. *Nature*, *421*(6926), 904–905.

Gordon, A. L., & Bosley, K. T. (1991). Cyclonic gyre in the tropical south atlantic. *Deep Sea Research Part A. Oceanographic Research Papers*, *38*, S323–S343.

Hernández-Guerra, A., & Talley, L. D. (2016). Meridional overturning transports at 30 s in the indian and pacific oceans in 2002–2003 and 2009. *Progress in Oceanography*, *146*, 89–120.

Hogg, N. G., & Owens, W. B. (1999). Direct measurement of the deep circulation within the brazil basin. *Deep Sea Research Part II: Topical Studies in Oceanography*, *46*(1-2), 335–353.

Hogg, N. G., Siedler, G., & Zenk, W. (1999). Circulation and variability at the southern boundary of the brazil basin. *Journal of Physical Oceanography*, *29*(2), 145–157.

Houghton, J. T. (1996). *Climate change 1995: The science of climate change: Contribution of working group i to the second assessment report of the intergovernmental panel on climate change* (Vol. 2). Cambridge University Press.

Hummels, R., Brandt, P., Dengler, M., Fischer, J., Araujo, M., Veleda, D., & Durgadoo, J. V. (2015). Interannual to decadal changes in the western boundary circulation in the atlantic at 11 s. *Geophysical Research Letters*, *42*(18), 7615–7622.

Johns, W. E., Baringer, M. O., Beal, L., Cunningham, S., Kanzow, T., Bryden, H. L., Hirschi, J., Marotzke, J., Meinen, C., Shaw, B., et al. (2011). Continuous, array-based estimates of atlantic ocean heat transport at 26.5 n. *Journal of Climate*, *24*(10), 2429–2449.

Kanzow, T., Send, U., Zenk, W., Chave, A. D., & Rhein, M. (2006). Monitoring the integrated deep meridional flow in the tropical north atlantic: Long-term performance of a geostrophic array. *Deep Sea Research Part I: Oceanographic Research Papers*, *53*(3), 528–546.

Kersalé, M., Meinen, C. S., Perez, R. C., Le Hénaff, M., Valla, D., Lamont, T., Sato, O. T., Dong, S., Terre, T., van Caspel, M., et al. (2020). Highly variable upper and abyssal overturning cells in the south atlantic. *Science Advances*, *6*(32), eaba7573.

Kersalé, M., Perez, R. C., Speich, S., Meinen, C. S., Lamont, T., Le Hénaff, M., van den Berg, M. A., Majumder, S., Ansorge, I. J., Dong, S., et al. (2019). Shallow and deep eastern boundary currents in the south atlantic at 34.5 s: Mean structure and variability. *Journal of Geophysical Research: Oceans*, *124*(3), 1634–1659.

Killworth, P. D., Chelton, D. B., & de Szoeke, R. A. (1997). The speed of observed and theoretical long extratropical planetary waves. *Journal of Physical Oceanography*, *27*(9), 1946–1966.

Knorr, G., & Lohmann, G. (2003). Southern ocean origin for the resumption of atlantic thermohaline circulation during deglaciation. *Nature*, *424*(6948), 532–536.

Kundu, P. K., & Allen, J. (1976). Some three-dimensional characteristics of low-frequency current fluctuations near the oregon coast. *Journal of Physical Oceanography*, *6*(2), 181–199.

Larqué, L., Maamaatuaiahutapu, K., & Garçon, V. (1997). On the intermediate and deep water flows in the south atlantic ocean. *Journal of Geophysical Research: Oceans*, *102*(C6), 12425–12440.

Li, C. (2022). *Time series data analysis in oceanography: Applications using matlab*. Cambridge University Press.

Lozier, M. S., Bacon, S., Bower, A. S., Cunningham, S. A., de Jong, M. F., de Steur, L., Deyoung, B., Fischer, J., Gary, S. F., Greenan, B. J., et al. (2017). Overturning in the subpolar north atlantic program: A new international ocean observing system. *Bulletin of the American Meteorological Society*, *98*(4), 737–752.

Lumpkin, R., & Speer, K. (2007). Global ocean meridional overturning. *Journal of Physical Oceanography*, *37*(10), 2550–2562.

Macdonald, A. M., & Wunsch, C. (1996). An estimate of global ocean circulation and heat fluxes. *Nature*, *382*(6590), 436–439.

Macdonald, A. M. (1995). *Oceanic fluxes of mass, heat, and freshwater: A global estimate and perspective* [Doctoral dissertation, Massachusetts Institute of Technology].

McCarthy, G. D., Brown, P. J., Flagg, C. N., Goni, G., Houpert, L., Hughes, C. W., Hummels, R., Inall, M., Jochumsen, K., Larsen, K., et al. (2020). Sustainable observations of the amoc: Methodology and technology. *Reviews of Geophysics*, *58*(1), e2019RG000654.

McCartney, M. S., & Talley, L. D. (1984). Warm-to-cold water conversion in the northern north atlantic ocean. *Journal of Physical Oceanography*, *14*(5), 922–935.

Meinen, C. S., Speich, S., Perez, R. C., Dong, S., Piola, A. R., Garzoli, S. L., Baringer, M. O., Gladyshev, S., & Campos, E. J. (2013). Temporal variability of the meridional overturning circulation at 34.5 s: Results from two pilot boundary arrays in the south atlantic. *Journal of Geophysical Research: Oceans*, *118*(12), 6461–6478.

Moat, B. I., Smeed, D. A., Frajka-Williams, E., Desbruyères, D. G., Beaulieu, C., Johns, W. E., Rayner, D., Sanchez-Franks, A., Baringer, M. O., Volkov, D., et al. (2020). Pending recovery in the strength of the meridional overturning circulation at 26 n. *Ocean Science*, *16*(4), 863–874.

Peterson, R. G., & Stramma, L. (1991). Upper-level circulation in the south atlantic ocean. *Progress in oceanography*, *26*(1), 1–73.

Preisendorfer, R. (1988). Principal component analysis in meteorology and oceanography. *Elsevier Sci. Publ.*, *17*, 425.

Rahmstorf, S., Box, J. E., Feulner, G., Mann, M. E., Robinson, A., Rutherford, S., & Schaffernicht, E. J. (2015). Exceptional twentieth-century slowdown in atlantic ocean overturning circulation. *Nature climate change*, *5*(5), 475–480.

Reid, J. L. (1989). On the total geostrophic circulation of the south atlantic ocean: Flow patterns, tracers, and transports. *Progress in Oceanography*, *23*(3), 149–244.

Reid, J. L., Nowlin, W. D., & Patzert, W. C. (1977). On the characteristics and circulation of the southwestern atlantic ocean. *Journal of Physical Oceanography*, *7*(1), 62–91.

Schmitz, W. (1996). On the world ocean circulation: Volume i. *Some Global Features/North Atlantic Circulation, Woods Hole Oceanographic Institution Technical Report WHOI-96-03*.

Sévellec, F., & Sinha, B. (2018). Predictability of decadal atlantic meridional overturning circulation variations. *Oxford Encyclopedia of Climate Science, Oxford University Press*.

Shanmugam, G. (2003). Deep-marine tidal bottom currents and their reworked sands in modern and ancient submarine canyons. *Marine and Petroleum Geology*, *20*(5), 471–491.

Shannon, L., Lutjeharms, J., & Agenbag, J. (1989). Episodic input of sub-antarctic water into the benguela region.

Shepard, F. P., Marshall, N. F., McLoughlin, P. A., & Sullivan, G. G. (1979). Currents in submarine canyons and other seavalleys.

Sloyan, B. M., & Rintoul, S. R. (2001). The southern ocean limb of the global deep overturning circulation. *Journal of Physical Oceanography*, *31*(1), 143–173.

Speer, K. G., & Zenk, W. (1993). The flow of antarctic bottom water into the brazil basin. *Journal of Physical Oceanography*, *23*(12), 2667–2682.

Srokosz, M., Baringer, M., Bryden, H., Cunningham, S., Delworth, T., Lozier, S., Marotzke, J., & Sutton, R. (2012). Past, present, and future changes in the atlantic meridional overturning circulation. *Bulletin of the American Meteorological Society*, *93*(11), 1663–1676.

Stramma, L., & England, M. (1999). On the water masses and mean circulation of the south atlantic ocean. *Journal of Geophysical Research: Oceans*, *104*(C9), 20863–20883.

Strub, P., Shillington, F., James, C., & Weeks, S. (1998). Satellite comparison of the seasonal circulation in the benguela and california current systems. *African Journal of Marine Science*, *19*.

Taft, B. A. (1963). Distribution of salinity and dissolved oxygen on surfaces of uniform potential specific volume in the south atlantic, south pacific, and indian oceans.

Talley, L. D. (2011). *Descriptive physical oceanography: An introduction*. Academic press.

Thomson, R. E., & Emery, W. J. (2014). *Data analysis methods in physical oceanography*. Newnes.

Thomson, R. E., Mihály, S. F., Rabinovich, A. B., McDuff, R. E., Veirs, S. R., & Stahr, F. R. (2003). Constrained circulation at endeavour ridge facilitates colonization by vent larvae. *Nature*, *424*(6948), 545–549.

Veirs, S. R. (2003). *Heat flux and hydrography at a submarine volcano: Observations and models of the main endeavour vent field in the northeast pacific* [Doctoral dissertation, University of Washington].

Warner, M. J., & Weiss, R. F. (1992). Chlorofluoromethanes in south atlantic antartic intermediate water. *Deep Sea Research Part A. Oceanographic Research Papers*, *39*(11-12), 2053–2075.

Wefer, G., Berger, W. H., Siedler, G., & Webb, D. J. (2012). *The south atlantic: Present and past circulation*. Springer Science & Business Media.

Weijer, W., De Ruijter, W. P., & Dijkstra, H. A. (2001). Stability of the atlantic overturning circulation: Competition between bering strait freshwater flux and agulhas heat and salt sources. *Journal of Physical Oceanography*, *31*(8), 2385–2402.

Weijer, W., De Ruijter, W. P., Sterl, A., & Drijfhout, S. S. (2002). Response of the atlantic overturning circulation to south atlantic sources of buoyancy. *Global and Planetary Change*, *34*(3-4), 293–311.

Wunsch, C. (2002). What is the thermohaline circulation? *Science*, *298*(5596), 1179–1181.

Wust, G. (1935). Schichtung und zirkulation des atlantischen ozeans. deutsche atl. exped."meteor" 1925–1927.